UC San Diego
UC San Diego Electronic Theses and Dissertations

Title
Development in CMOS-compatible materials for on-chip nonlinear optical devices

Permalink
https://escholarship.org/uc/item/335800wm

Author
Lin, Hung-Hsi

Publication Date
2018

Peer reviewed|Thesis/dissertation

eScholarship.org Powered by the California Digital Library
University of California

UNIVERSITY OF CALIFORNIA, SAN DIEGO

# Development in CMOS-compatible materials for on-chip nonlinear optical devices

A dissertation submitted in partial satisfaction of the

requirements for the degree Doctor of Philosophy

in

Materials Science and Engineering

by

Hunghsi Lin

Committee in charge:

Professor Yeshaiahu Fainman, Chair
Professor Eric Edward Fullerton
Professor Andrew Kummel
Professor Yu-Hwa Lo
Professor Paul Yu

2018

Copyright

Hunghsi Lin, 2018

All rights reserved.

The Dissertation of Hunghsi Lin is approved, and is acceptable in quality and form for publication on microfilm and electronically:

---

---

---

---

---

Chair

University of California, San Diego

2018

TABLE OF CONTENTS

Signature Page ... iii

Talbe of Contents ... iv

List of Figures ... vi

List of Tables ... x

Acknowledgements ... xi

Vita… ... xiii

Abstract of the Dissertation ... xv

Chapter 1 Introduction ... 1

Chapter 2 Engineered metamaterials for efficient optical nonlinear processes ... 9
- 2.1 Background ... 10
- 2.2 Materials and Methods ... 11
  - 2.2.1 Fixed charges generated at dielectric/semiconductor interfaces ... 11
  - 2.2.2 Engineered built-in electric field within semiconductor via asymmetrical claddings ... 14
  - 2.2.3 Metamaterials consisit of dielectric/semiconductor/dielectric stacks ... 15
- 2.3 Results ... 17
- 2.4 Discussion ... 24
- 2.5 Conclusion ... 25
- Acknowledgements ... 26

Chapter 3 Metamaterials with engineered tuanable optical nonlinearities ... 27
- 3.1 Background ... 27
- 3.2 Materials and Methods ... 28
  - 3.2.1 Junction generated at metal/semiconductor interfaces ... 28
  - 3.2.2 Engineered built-in electric field within semiconductor via asymmetrical metal claddings ... 29
  - 3.2.3 Metamaterials consisit of metal/semiconductor/metal stacks ... 30
- 3.3 Results ... 32
- 3.4 Discussion ... 40
- 3.5 Conclusion ... 41
- Acknowledgments ... 42

Chapter 4 Silicon-rich nitride for nonlinear optical processes ... 43
- 4.1 Background ... 43

4.2 Materials and Methods ........................................ 44
4.2.1 Nonlinearities in silicon nitride ........................................ 44
4.2.2 Optical properties in silicon-rich nitride ........................................ 45
4.2.3 Enhanced second-order nonlinearity in silicon-rich nitride ........................................ 46
4.3 Results ........................................ 47
4.4 Discussion ........................................ 52
4.5 Conclusion ........................................ 54
Acknowledgments ........................................ 55

Chapter 5 Conclusion and Future Works ........................................ 56

Appendix A. C-V measurements ........................................ 59
A.1 Background ........................................ 59
A.2 Materials and Methods ........................................ 59
Acknowledgments ........................................ 60

Appendix B. Maker fringes setup ........................................ 61
B.1 Background ........................................ 61
B.2 Materials and Methods ........................................ 62
Acknowledgments ........................................ 64

Appendix C. Maker fringes analysis for MSM metamaterials ........................................ 65
C.1 Background ........................................ 65
C.2 Materials and Methods ........................................ 67
C.3 Analysis of the effect of photocurrent on the built-in electric field withing a-Si layer. ........................................ 68
Acknowledgments ........................................ 70

Bibliography ........................................ 72

LIST OF FIGURES

**Figure 2.1**: The electric field distribution within a silicon waveguide when the cladding material is silicon nitride. The spatial dimensions are indicated in units of microns. ........................................................................................12

**Figure 2.2**: (a) The schematic of DSD metamaterial consisting of multiple periods of $Al_2O_3$/a-Si/$SiO_2$. (b) C-V curves for extraction of Qf at $Al_2O_3$/a-Si and $SiO_2$/a-Si interfaces at 10kHz ......................................................................14

**Figure 2.3**: Simulated electric field within the 25nm a-Si layer in symmetrical (black solid curve) and asymmetrical (red solid curve) DSD metamaterials. The blue dashed line shows that the net electric field is zero for the symmmetrical case. ........................................................................................................15

**Figure 2.4**: The generated (combination of p- and s-polarized) second-harmonic responses versus pump power from one (blue triangles) and two periods (black circles) of the asymmetrical DSD stack plot on a log-log scale. (b) The p- and s-polarized second-harmonic signals generated from one and two periods of the asymmetrical metamaterials (blue for one period and black for two periods of the DSD stack; solid lones for generated p- and dashed lines for generated s-polarized SHG responses) and two cycles of the symmetrical DSD stack (red) under variant polarization angles of pump light, where the average power is 150 mW with a fixed incident angle of 45 degrees. ...........18

**Figure 2.5**: C-V measurements on (a) $SiO_2$/a-Si and (b) $Al_2O_3$/a-Si interfaces for as-deposited (black), 200$^o$C (red), 300$^o$C (green), and 400$^o$C (blue) annealed samples. The generated p-polarized SHG signals from (c) one and (d) two periods of asymmetrical DSD metamaterials at different temperatures of annealing treatment with variant polarization angles of the incident laser. ...21

**Figure 2.6**: The calculated $Q_f$ in $SiO_2$/Si (blue boxes) and $Al_2O_3$/Si (red boxes) interfaces and the extracted effective $\chi^{(2)}_{zzz}$ in one (brown circles) and two (green squares) periods of asymmetrical metamaterials.. .......................................22

**Figure 2.7:** Calculated mode for DSD metamaterials at the wavelength of 1.55 micro-meters. (b) Ring resonator waveguide structure fabricated using DSD metamaterials. ........................................................................................23
**Figure 2.8:** STEM figures of DSD metamaterials deposited by a magnetron sputter machine. ........................................................................................23
**Figure 3.1:** (a) The schematic of a MSM metamaterial consisting of a-Si clad with two different metals, metal A and metal B. (b) The reduced band diagram of a-Si, metal A and metal B without intimate contact. (c) The reduced band diagram of symmetrical and (d) asymmetrical MSM structures under equilibrium with intimate contact. ........................................................................................30
**Figure 3.2:** (a) Schematic and SEM image of a 5 nm Ni/ 25nm a-Si/5 nm Al MSM metamaterial for second-harmonic generation process. (b) Reduced band diagram and the simulated distribution of built-in electric field for the Ni/a-Si/Al metamaterial. ........................................................................................31
**Figure 3.3:** Transmission of TM-(a) and TE-(b) polarization of one and two periods of Al /a-Si / Ni stack under variant incident angles with wavelength at 400 nm and 800 nm. ........................................................................................32
**Figure 3.4:** (a) Log-log plot of measured SHG signal versus pump power for a single layer of Al (red triangles), Ni (blue squares) films and MSM metamaterial (black circles) grown on silica substrates for a fixed pump beam incident angles of 45$^{o}$. (b) Generated p-polarzied and (c) s-polarized SHG intensity versus polarization angle for a 100 mW pump. ...........................................34
**Figure 3.5:** Measured SHG intesnities from the Ni/a-Si/Al (left) and Pt/a-Si/Al (right) MSM metamaterials and their constituents. The red boxes show the SHG from a single layer of Al film, and the blue boxes show the SHG from top cladding metal films. The difference between the total measured SHG intensities from the MSM metamaterials and the their components is then assumed to be from the bulk of the a-Si (yellow) layer via EFISH effect. ....35
**Figure 3.6:** (a) Schematic of an active MSM material. (b) Measured SHG intensity under variant DC voltage (dots), and the red fitting curve showing the quadratic

dependency. (c) Schematic representing the design for creating spatial nonlinear responses, and the top-view SEM image of the fabricated metal grating. (d) SHG intensity from the patterned MSM structure detected under different angles and external electrical biases ............................................40

**Figure 4.1:** (a) Schematic of Maker fringes setup. (b) Variation of the second-harmonic signal for 200 and 500 nm thick $SiN_x$ as a function of polarization angle for the two case of s- and p- polarized input pump. ..........................................45

**Figure 4.2:** (a) SEM image of the silicon nitride waveguide. (b) Measured TE second-harmonic power generated in a 1070 nm-wide silicon nitride waveguide, as a function of the pump wavelength................................................................46

**Figure 4.3:** EDX results on the sample of (a) S1, (b) S2 and (c) S3. .............................49

**Figure 4.4:** (a) Composition of sample S1, S2 and S3 investigated by energy dispersive X-ray (EDX) microanalysis, the inset figures is the example of measured EDX data on sample S3. (B) The p- (black squares) and s- (red squares) generated SHG signals from S3 under variant incident polarization angles. (c) The p-(black squares) and s- (red circles) generated SHG signals from S3 under variant incident polarization angles. ................................................49

**Figure 4.5:** SEM micrograph of an unclad SRN waveguides showing the waveguide cross-section and the coupling region of the ring-resonators. .......................51

**Figure 4.6:** Normalized transmission of a 1 um wide SRN waveguide coupled to a ring-resonator at a coupling gap of 250 nm. The inset shows the corresponding mode profile of the fundamental TE mode and a singe resonance at 1520 nm, used to estimate the loss-coefficient of these waveguides............................52

**Figure 4.7:** (a) Schematic of reflective second-harmonic generation setup. (b) The generated SHG signals from sample at the wavelength of 1040 nm (red bars) and 1550 nm (blue bars), respectively........................................................53

**Figure S.1:** Schematic of Maker fringes setup for optical characterization.....................62

**Figure S.2:** EDX results of a-Si grwon on (a) sapphire and (b) fused silica...................63

**Figure S.3:** (a) Schematic of the patterned MSM stack for measurement of I-V behaviors under different illumination conditions. (b) I-V behaviors without (black) and with illumination under variant average power. ..........................................70

LIST OF TABLES

**Table 2.1:** Calculated components of the effective $\chi^{(2)}$ tensors......................................19

**Table 3.1:** Calculated components of the effective $\chi^{(2)}$ tensors in MSM metamaterials ..36

**Table 4.1:** Calculated components of the effective $\chi^{(2)}$ tensors in silicon nitride with variant thickness..........................................................................................45

**Table 4.2:** The deposition recipes and measured properties of silicon nitride thin films. 50

**Table S.1:** Real and imaginary part of refractive index for dielectrics and a-Si thin films measured using elliposometer at 400 nm and 800 nm. .................................64

**Table S.2:** Real and imaginary part of refractive index for metal and a-Si thin films measured using elliposometer at 400 nm and 800 nm. .................................67

**Table S.3:** Electrical properties of a-Si layer under variant illumination conditions. ......70

# ACKNOWLEDGEMENTS

This would not happen without my committee member, great assistance from colleagues and lab mates, also supports from my friends and family.

I would like to express my deepest appreciation to my advisor, Dr. Fainman, for his guidance and support to my research in past five years. Also thanks Dr. Fullerton for his assistance on experiments in material growth. I would like to also thank Dr. Yu, Dr. Lo, and Dr. Kummel for their participation in my committee and providing valuable suggestions for my study.

I especially want to thank all members in Shaya's group, Mu-Han, Cheng-Yi, Rajat, Matt, Felipe, Christian, Karim, Shiva, Faraz and Alex, who were always willing to help and provide advice to my research. Also, I would like to thank Dr. Shubin for building my fabrication related backgrounds.

Finally, I would like to thank my parents and my younger sister for their great support and best wishes. My girlfriend, Hannah Yang, was always there stood by me through the hardest times. This dissertation is dedicated to the endless love from my family.

Chapter 2, in part, contains materials from "Synthesis of second-order nonlinearities in dielectric-semiconductor-dielectric metamaterials", published at Applied Physics Letters drafted by Hung-Hsi Lin, Mu-Han Yang, Rajat Sharma, Matthew Puckett, Christian Wurm, Sergio Montoya, Felipe Vallini, Eric Fullerton and Yeshaiahu Fainman. The dissertation author was the first author of the manuscript.

Chapter 3, in part, contains materials from "Electronic Metamaterials with Tunable Second-order Optical Nonlinearities", published at Scientific Reports drafted by Hung-Hsi Lin, Felipe Vallini, Mu-Han Yang, Rajat Sharma, Matthew Puckett, Christian Wurm,

Sergio Montoya, Eric Fullerton and Yeshaiahu Fainman. The dissertation author was the first author of the manuscript.

Chapter 4, in part, contains materials from "Observation of second-harmonic generation in silicon nitride waveguides through bulk nonlinearities" published at Optics Express by Matthew Puckett, Rajat Sharma, Hung-Hsi Lin, Mu-Han Yang, Felipe Vallini and Yeshaiahu Fainman. The dissertation author was co-author and in charge of measurements of second-order nonlinearity in silicon nitride in both free-space and in waveguide configuration. This part also contains materials from "On the nature of second-order nonlinearity in silicon nitride" which is in preparation for submission, the dissertation author is the first author of the manuscript.

Appendix A contains the C-V measurement from "Characterizing the effects of free carriers in fully etched, dielectric-clad silicon waveguides" published at Applied Physics Letters drafted by Rajat Sharma, Matthew Puckett, Hung-Hsi Lin, Felipe Vallini and Yeshaiahu Fainman, the dissertation author is the co-author and in charge of C-V analysis on dielectric properties.

Appendix B includes the supplementary materials from the paper mentioned in chapter 2, while the dissertation author is the first author.

Appendix C includes some supplementary materials based on the paper discussed in chapter 3, the dissertation author is the first author.

## VITA

2008 Bachelor of Science, National Tsing Hua University, Taiwan.

2011 Master of Science, National Tsing Hua University, Taiwan

2018 Doctor of Philosophy, University of California San Diego, La Jolla.

## PUBLICATIONS

Journal Article

- **H. Lin** and Y. Fainman et al., "Electronic Metamaterials with Tunable Second-order Optical Nonlinearities" Scientific Reports 7, 9983 (2017)
- **H. Lin** and Y. Fainman et al., "Synthesis of second-order nonlinearities in dielectric-semiconductor- dielectric metamaterials," Applied Physics Letters 110, 113103 (2017)
- M. W. Puckett, R. Sharma, **H. Lin**, M. Yang, F. Vallini, and Y. Fainman, "Observation of second- harmonic generation in silicon nitride waveguides through bulk nonlinearities," Opt. Express 24, 16923-16933 (2016)
- R. Sharma, M.W. Puckett, **H. Lin**, A. Isichenko, F. Vallini, and Y. Fainman, "Effect of dielectric claddings on the electro-optic behavior of silicon waveguides", Optics Letters 41, 6, (2016)
- R. Sharma, M.W. Puckett, **H. Lin**, F. Vallini and Y. Fainman, "Characterizing the effects of free carriers in fully etched, dielectric-clad silicon waveguides", Applied Physics Letters106, 241104 (2015)

Conference Paper

- **H. Lin**, R. Sharma, M. Yang, M. W. Puckett, C. D. Wurm, F. Vallini, Y. Fainman, "Enhanced Effective Second-order Nonlinearities in Si-rich SiNx Thin Films", CLEO (2017)
- Y. Fainman, M. Puckett, R. Sharma, **H. Lin**, and F. Vallini, "Effects of Dielectric Cladding on Si Nanophotonics", CLEO (2017)
- J. Davis, **H. Lin**, A. Grieco, and Y. Fainman, "Effect of Dielectric Interfaces on Second-Harmonic Generation in Integrated GaN Resonators", CLEO (2016)
- **H. Lin**, M. Yang, R. Sharma, M. W. Puckett, S. Montoya, C. Wurm, F. Vallini, E. Fullerton, and Y. Fainman, "Engineering of a Second-Order Nonlinearity in Silicon-Dielectric Multilayers", CLEO (2016)
- R. Sharma, M.W. Puckett, **H. Lin**, F. Vallini, and Y. Fainman, "Free carrier effects as a complicating variable in the analysis of strained silicon", IEEE Photonics Conference (2015)
- R. Sharma, **H. Lin**, M.W. Puckett, and Y. Fainman, "Realization of A SOI-Like III-V Platform Based On the Integration of GaAs With Silicon", CLEO (2015)

ABSTRACT OF THE DISSERTATION

Development in CMOS-compatible materials for on-chip nonlinear optical devices

by

Hunghsi Lin

Doctor of Philosophy in Materials Science and Engineering

University of California, San Diego, 2018

Professor Yeshaiahu Fainman, Chair

Silicon photonics is a system that utilizes silicon as an optical medium and photon as carriers for communicating application. The operating wavelength of silicon photonic system is typically at 1.55 micormeter which has been used by most fiber telecommunication systems. The components on the silicon photonic are usually patterned in sub-micron precision using technologies that are available from current electronic industry. With the functionalities from variant components on silicon photonic platform, including source, coupler, amplifier, modulator and detector, the silicon photonic chip has the capability to carry, modulate, deliver specific optical information efficiently. Theoretically, faster, larger amount of information can be delivered in optical platform

compared to current used electrical system.

Optical modulator is a device used for modulating the shape and amplitude of the traveling light. Modulators can be categorized into phase modulators, polarization modulators and amplitude modulators dependent on the changed parameters, and the modulators can also be divided into absorptive and refractive type modulators based on the properties of material that is manipulated. Refractive modulators has the benefits in low loss compared the absorption type modulators, and in the silicon photonic field, electro-optic effect is preferred because of better efficiency than other effect like acousto-optic effect.

The electro-optic effect means the electric field induced change on optical properties in a material. Current technique for efficient electro-optic effect based modulator includes the use of Pockels and Kerr effects, which utilizes materials' second- and third-order optical nonlinear properties, respectively. Both effect produces changes of refractive in an optical medium induced by an electric field, while the change from Pockels effect is proportional to the electric field and Kerr effect is proportional to the square of the field. The Pockels effect occurs only in crystals that lack of inversion symmetry while all materials show Kerr effect. Crystal materials like lithium niobate and gallium arsenide exhibit large second-order nonlineaity for Pockels effect, however, these materials are not CMOS-compatible and have challenges to be integrated on the current silicon photonic platforms.

Even though silicon and most dielectric materials used in electronic industry inherently has zero second-order nonlinearity for performing Pockels effect, there are still alternative ways to engineer nonlinearities in these CMOS compatible materials, such as

strained technique, electric field induced second-harmonic generation, asymmetry from the interfaces and introduction of silicon nanoclusters. These ways have been already investigated and proved as methods to change and synthesize material's both optical linear and nonlinear properties.

Overall, this thesis presents the contributions to systematical study on the engineered optical nonlinear properties in the metamaterials, composed by CMOS-compatible materials, and also another recently developed dielectric, silicon-rich nitride. The large and tunable optical nonlinearities of these materials have already shown great potential for efficient nonlinear devices. It is believed that with further optimization on the material selection and fabrication, the proposed metamaterials and silicon nitride based materials can be widely used in the fields of on-chip light modulation, switching and light conversion.

# CHAPTER 1

# INTRODUCTION

Silicon has been a primary candidate for integrated photonics because of its matured techniques in electronic industry. Silicon is also a material which is optical transparent at 1550 nm where the wavelength that fiber telecommunication widely used, along with the reported low loss in waveguide configuration [1,2], making it become a great candidate for on-chip optics component. The core components on the silicon photonics includes the light source, which is used for the generation of light, in other words, the photon carriers. Then a waveguide exhibiting the ability to guide the light with low loss and good optical field confinement is also required. The light initially carries meaningless information, a modulator is needed to transfer this light into meaningful spectrum. And this optical signal will be detected by a photodetector, then read by computer. Finally, all these components will be assembled on the silicon based platform.

The modulator used for manipulating the shape and magnitude of the light requires strictly good efficiency for low power consumption and compactness of the device. Acoustic, thermal and electrical methods are most common ways for modulating the light wave. Among these techniques, electro-optic way introduces the benefits of faster and more efficient. Therefore, to find the CMOS-compatible materials for electro-optic type modulation attracts lots of attention for silicon phonics. However, one if its shortcomings for these materials comes from the lack of second-order nonlinearity susceptibility ($\chi^{(2)}$),

which can be used for efficient modulation via Pockels effect [3]. The zero second-order nonlinearity in silicon results from its diamond lattice centrosymmetry structure, disallowing the application of this material for modulation via $\chi^{(2)}$ processes [4]. To overcome this inherent materials challenge, some works over the past decades have been developing strain-induced second-order nonlinearity for silicon based device [5-7]. The induced nonlinearity originates from breaking symmetry in silicon by cladding a highly stressed thin film (i.e., silicon nitride) on top of silicon waveguide, related works has been reported in both theory and experiment, showing the potential of this technique for on-chip modulation using Pockels effect [8,9]. The value was reported to be as high as 330 pm/V, even larger than lithium niobate ($LiNbO_3$) which has been widely used for nonlinear processes [10].

However, it was found that the change of the modulation of optical signals in strained silicon platform doesn't not only contribute from the strained induced breaking symmetry, the overall effect is the combination of four mechanisms listed below:

*(A) Strained induced second-order nonlinearity.*

Strained in silicon via silicon nitride ($SiN_x$) cladding layer has been proved to exhibit nonlinearities [11].

*(B) Electric field induced second-harmonic generation (EFISH)*

EFISH effect has been proved to contribute on second-order nonlinear process while there is an induced static electric field interacting with material's third-order nonlinearity [12].

*(C) Silicon nitride*

Silicon nitride has been proved to exhibit non-zero second-order nonlinearity despite of its amorphous nature [13].

*(D) Free carrier effect*

For active devices, the applied voltage does not only change the field within silicon waveguide, the free carriers in silicon are also changed, consequently the optical properties are simultaneously changed based on Soref's equation [14].

To develop the most efficient way for optical modulation utilizing Pockels effect, it is important to decouple and estimate the contribution of each mechanisms to the modulation behavior, and then determine the most dominating factor in this strained induced nonlinearity technique.

First, the strained induced nonlinearity has been proved to be no more than 8 pm/V at 1550 nm [11]. To exclude any contribution from the silicon nitride cladding layer or from the fixed charge induce nonlinearity, the silicon waveguide is strained mechanically using a customized device. Based on the simulation of strain gradient in silicon and experimental results on high speed measurement, it is concluded that the strained induced nonlinearity in silicon is less than 10 pm/V, which is an order smaller than proposed value in strained silicon platform [8-10].

Silicon nitride is a material which exhibits high stress within thin film, and it has been used as the source for introducing strain in silicon waveguide. At the interface between dielectric layer and semiconductor, the fixed charge ($Q_f$) and interface trap ($D_{it}$) are always generated within the dielectric, then create a static electric field in semiconductor, the vector and magnitude of the built-in field is dependent on the polarity and amount of the charges [15]. Silicon nitride has been reported as a dielectric which

exhibits larger amount of $Q_f$ than silicon oxide ($SiO_2$), therefore, a large field in silicon waveguide induced by the charges can be expected in strained silicon platform. This generated field then interacts with materials third-order nonlinear susceptibility ($\chi^{(3)}$), results in an effective $\chi^{(2)}$ following by the equation [16]:

$$\chi_{eff}^{(3)} = 3 \times \chi^{(2)} \times E_{DC} \quad (1)$$

where the $E_{DC}$ is the static electric field, coming from the fixed charges generated within dielectrics. Based on this equation with the reported value of fixed charges, an effective $\chi^{(2)}$ of 11.6 pm/V is expected in silicon nitride clad silicon waveguide [12]. To prove the measured second-harmonic generation (SHG) is mostly from EFISH effect, a silicon waveguide clad with high stress $SiO_2$ is also investigated, the result shows that the SHG intensity from this case is far lower compared to the case with $SiN_x$ cladding, proves the fact that EFISH is the dominating factor instead of the strain.

Besides the EFISH and strain effect, the cladding layer, silicon nitride itself was found as a source of $\chi^{(2)}$ contributor. M. Lipson's group first reported experimental second-harmonic generation and third-harmonic generation (THG) from $SiN_x$ ring resonators, and the source of $\chi^{(2)}$ was attributed to the non-zero polarization at interface of $SiN_x$ [17]. $SiN_x$ was generally deposited using sputter, plasma enhanced chemical vapor deposition (PECVD) or low pressure chemical vapor deposition (LPCVD), formed as amorphous structure. Since the nature of deposited amorphous structure, the $SiN_x$ theoretically exhibits symmetry and isotropic polarizations in its bulk of material. However, T. Ning in 2012 first claimed on the discovery of non-zero $\chi^{(2)}$ with the value of 2 pm/V in bulk of PECVD deposited $SiN_x$ [13], and then this find was also confirmed by many other groups [18-20]. Our group first demonstrate the in-waveguide second-harmonic generation in $SiN_x$

waveguide, supporting the hypothesis on existence of nonlinearity in bulk of silicon nitride instead of interface [21]. Therefore, $SiN_x$ should be seen as one of source contributing to the nonlinear process in strained silicon platform.

From the mechanisms described above, the contribution to $\chi^{(2)}$ from strain, EFISH and silicon nitride is roughly 8, 11, and 2 pm/V, respectively. It is not able to explain the overall measured $\chi^{(2)}$, which is at hundreds of pm/V in strained silicon system. We then thoroughly studied the modulation behavior resulting from free carrier effect, found that in fact it is the dominating factor causing the large change of refractive index [22]. Instead of utilizing $\chi^{(2)}$, the free carrier effect mechanism changes the optical properties via manipulating the carrier concentration within the waveguide. We found that while applying external voltage source, the electric field for triggering Pockels effect hardly penetrates into silicon waveguide. On the other hand, a dramatic carrier distribution was observed from Silvaco simulation results, which introduces the change of refractive index and absorption coefficient. Therefore, we deduced that the change of refractive index measured from strained silicon platform is mostly from the free carrier plasma dispersion effect instead of Pockels effect using material's $\chi^{(2)}$. This hypothesis was confirmed through a systematic study with Soref's theory, Silvaco simulation and experimental verification which is published by our group [22, 23]. Even though free carrier effect can be an efficient source for optical modulation, the drawbacks of loss and speed issues hinder the application in modulator which requires the characterization of high speed and low loss.

To utilize the Pockels effect, which exhibits high speed and low loss potentials, developing materials which has $\chi^{(2)}$ becomes an important task. However, existing materials that exhibit large $\chi^{(2)}$ (e.g., lithium niobate ($LiNbO_3$) and potassium dihydrogen

phosphate (KDP) crystals) are not compatible with CMOS technology [24-26]. Single-crystalline silicon is prohibited to exhibit non-zero electrical dipole induced $\chi^{(2)}$ due to the nature of its centro-symmetrical lattice. Still, second-harmonic responses can be generated if quadrupolar and magnetic dipoles are considered [27,28]. However, the demonstrated conversion efficiencies are relatively small compared to bulk effects of commonly used nonlinear crystals. Additionally, CMOS- compatible dielectric materials such as aluminum oxide ($Al_2O_3$) and silicon dioxide ($SiO_2$) are reported to have extremely low $\chi^{(2)}$ because of their amorphous nature [29,30]. Therefore, the need for CMOS-compatible materials exhibiting prominent $\chi^{(2)}$ that can be easily integrated with modern silicon photonic material platforms is highly desirable.

Metamaterials have attracted significant attention because their physical properties can be synthesized with the selection of materials and their spatial distributions [31,32]. Metal-dielectric multilayers exhibit plasmonic-enhanced $\chi^{(2)}$ values resulting from the interface between metal and dielectric layers [33], and the effective $\chi^{(2)}$ can be further increased via charging the density of electrons at the surface of metals by applying an external DC electric field [34]. However, the use of metals leads to high optical insertion loss in the fabricated device. To overcome the loss issue, Alloatti et al. demonstrated an all-dielectric ABC metamaterial that exhibits $\chi^{(2)}$ and consists of three different dielectric layers deposited by atomic layer deposition (ALD) [30] where the symmetry is broken via introducing asymmetry of surface density states on their interfaces, and the value of the reported highest component of the $\chi^{(2)}$ tensor, $\chi^{(2)}_{zzz}$, is 0.26 pm and Clemmen et al. modified the calculations and claimed that the value of $\chi^{(2)}_{zzz}$ based on the concept of all-dielectric metamaterials can be as high as 5 pm/V [35]. A larger value of $\chi^{(2)}$ is also claimed

to be achievable in this type of metamaterial via choosing the dielectric materials that exhibit high asymmetries in the density of their surface interfaces; however, these surface states existing in high density of interfaces also act as trapping centers, resulting in higher optical losses [36].

This thesis focuses mostly on the CMOS-compatible $\chi^{(2)}$ material development for on-chip nonlinear optical devices, utilizing the concept of metamaterials via the mechanisms of EFISH effect and also the silicon-rich nitride technique.

Chapter 2 describes the concept of metamaterial composed by the stack of dielectric/semiconductor/dielectric, where the nonlinearity was engineered through EFISH effect. The required statistic field for EFISH effect originates from the generated charges at the interface of dielectric and semiconductor. The theory, simulation and experimental results of this proposed metamaterial will be systematically discussed.

Chapter 3 addresses another idea of metamaterial composed by the stack of metal/semiconductor/metal, the mechanism of optical nonlinearity from this metamaterial is also from EFISH effect. The benefit of this type of metamaterial is the tunability of nonlinearity, and the property can be used for switching application. Besides, the idea of generating spatial distribution of second-harmonic generation signal is also demonstrated by simply patterning one side of electrode metal layer.

Chapter 4 exhibits a study of nonlinearity in silicon nitride and silicon-rich nitride. As a CMOS-compatible material, the existence of nonlinearity in $SiN_x$ make it as great candidate for on-chip nonlinear devices. The nonlinearity is experimentally verified via SHG in both free-space and waveguide configuration, the influence of silicon percentage in $SiN_x$ on optical properties is also studied.

Chapter 5 summarizes the contributions of this dissertation and discusses possible future research directions.

# CHAPTER 2

# ENGINEERED METAMATERIALS FOR EFFICIENT OPTICAL NONLINEAR PROCESSES

Optical materials with large second-order nonlinear susceptibility are essential for the construction of high speed photonic devices that need to be integrated into photonic integrated circuits (PIC) to realize functionalities such as ultrafast modulation, switching, and nonlinear wave mixing of optical fields on a chip. The current trend in fabrication of PICs is focused on developing optical materials that are compatible with cost effective CMOS manufacturing processes. Silicon has long been the material of choice for integrated photonics due to its prevalence in the electronics industry [37], its transparency in the near-IR wavelength regime [38], and its large third-order nonlinear susceptibility [39]. However, it suffers from two-photon absorption, limiting its efficiency in nonlinear wavemixing applications [40]. Moreover, due to its centrosymmetry, silicon lacks the second-order nonlinear susceptibility ($\chi^{(2)}$), preventing the possibility for efficient modulation and switching based on the Pockels effect, as well as three-wave mixing processes[41]. A substantial body of research has focused on circumventing or removing this shortcoming [5-8] by creating or engineering a strain gradient for breaking the inversion symmetry of

the silicon lattice, however, the resulting ($\chi^{(2)}$) coefficients are both controversial and extremely small.

Most CMOS-compatible dielectric materials have extremely low $\chi^{(2)}$ because of their amorphous nature. In this chapter, I will demonstrate a concept on engineered large effective second-order nonlinear optical susceptibility in electronic optical metamaterials based on the structured of sputtered dielectric-semiconductor-dielectric (DSD) multilayers of silicon dioxide/amorphous silicon/aluminum oxide [42].

## 2.1 Background

The main mechanism of the DSD metamaterial is from the EFISH effect. The EFISH effect offers an alternative way to engineer effective $\chi^{(2)}$ in materials by exploiting their $\chi^{(3)}$ even though the composites are the materials with zero or low $\chi^{(2)}$. The induced effective $\chi^{(2)}$ through this effect has been demonstrated theoretically and experimentally, in both metal-semiconductor (MS) and metal-oxide-semiconductor (MOS) structures. However, the penetration field in silicon from typical MS or MOS structures is too shallow for efficient nonlinear process, the reason will be explicitly explain in next section. In order to utilize this effect more effectively, a dielectric- semiconductor-dielectric (DSD) metamaterial consisting of a semiconductor thin film (i.e., a-Si) cladded with two different dielectric layers (i.e., $SiO_2$ and $Al_2O_3$) was proposed and studied. We exploit the creation of fixed charges ($Q_f$) of opposite signs on the surfaces of the semiconductor in the DSD multilayer structure to engineer and maximize a non-zero built-in electric field within the

a-Si layer, which in turn interacts with $\chi^{(3)}$ of the semiconductor, resulting in an enhanced, effective $\chi^{(2)}$ in the bulk of the metamaterial.

## 2.2 Materials and Methods

### 2.2.1 Fixed charges generated at dielectric/semiconductor interfaces

When a dielectric layer is deposited on a semiconductor, the semiconductor's valence and conduction band energies may locally deviate from their bulk values due to the existence of surface charges in the dielectric layer, leading to perturbations away from the material's bulk carrier distributions. At the dielectric/semiconductor interfaces, the neutral atoms in the dielectric layer tend to donate mobile electrons or holes into the semiconductor, leaving fixed charges at the dielectric side, which then create a space charge region within the semiconductor, resulting in a depletion region. Different dielectrics exhibit dissimilar polarities and densities of $Q_f$ at their interfaces with the same semiconductor, causing different electrical properties in the induced depletion regions.

To investigate the fixed charge induced SHG in strained silicon platform, a simulation of field distribution in a waveguide structure was performed, as shown in figure 2.1, using the semiconductor device physical tool, TCAD SILVACO [43]. It shows the case which has silicon nitride as the cladding layer: a high electric field is built closed to the surface of the silicon waveguide and the highest magnitude is $1x10^5$ V/cm, which is close to the breakdown voltage of silicon. The electric field decreases dramatically away from the surface of silicon, and most of the high built-in field locates only within tens of nanometer from the interface between the dielectric and the semiconductor, affecting the

propagating optical mode. These $Q_f$ induced built-in electric field has been shown to have influences on in-waveguide SHG via the EFISH effect, however, small overlap between the guiding mode and the high induced $\chi^{(2)}$ makes the light conversion extremely inefficient.

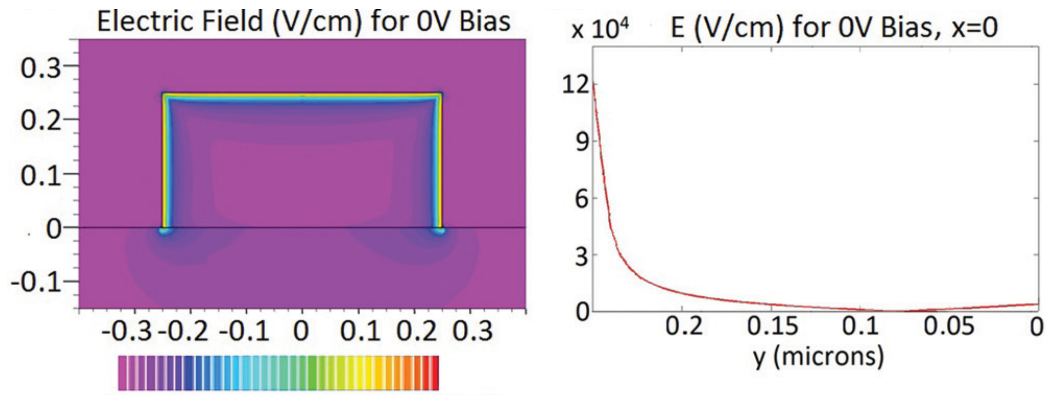


Figure 2.1: The electric field distribution within a silicon waveguide when the cladding material is silicon nitride. The spatial dimensions are indicated in units of microns. [22]

We have shown theoretically how dielectric claddings impact the electric field within the silicon waveguides. These results are significant because they clearly indicate that the distribution of $Q_f$ can be engineered to induce an effective $\chi^{(2)}$ in silicon waveguides and has potential for realization of CMOS-compatible electro-optic modulators and wave-mixers which do not rely on the injection of electrical currents, which cause Joules loss. However, our simulation results show that the charge induced fields are located only within tens of nanometers from the interfaces, which results in low effective $\chi^{(2)}$ for a relatively large area optical mode in the Si waveguide. A structure exhibiting a high and constant static electric field through the entire optical mode area in the bulk of the waveguide would be ideal for efficient on-chip nonlinear applications.

Intuitively, when a thin film of the semiconductor is cladded with different dielectrics with opposite polarities at either sides, the larger asymmetry of $Q_f$ results in a higher built-in electric field and a more prominent effective $\chi^{(2)}$ in the semiconductor. Therefore, we propose to exploit different polarities of these fixed charges on semiconductor interfaces to maximize the nonlinear optical properties of the metamaterial structures consisting of multiple periods of asymmetrical DSD thin film stacks as shown in figure 2.2(a), where an a-Si thin layer is cladded with $SiO_2$ and $Al_2O_3$. The thin thickness of the a-Si layer is fundamentally important to create a constant high static induced electric field within the semiconductor layer, enhancing the average effective $\chi^{(2)}$ in the bulk of the DSD stack. To characterize the $Q_f$ presented at the two semiconductor-dielectric interfaces, the most common technique is to analyze the capacitance-voltage (C-V) behavior of a MOS structure consisting of the dielectric materials of interest. Two test samples were fabricated for characterizing $Q_f$ at $SiO_2$/a-Si and $Al_2O_3$/a-Si interfaces (Appendix A: C-V measurement). The experimental results showing C-V curves performed at 10 kHz are displayed in figure 2.2(b). The calculated $Q_f$ densities are determined to be $1x10^{12}$ $cm^2$ and $2x10^{12}$ $cm^2$ for $SiO_2$ and $Al_2O_3$, respectively. The measured different signs and quantities of $Q_f$ from these two dielectrics are expected to cause a large non-zero gradient of field distribution within the a-Si thin film, supporting the fundamental concept of nonlinear DSD metamaterials.

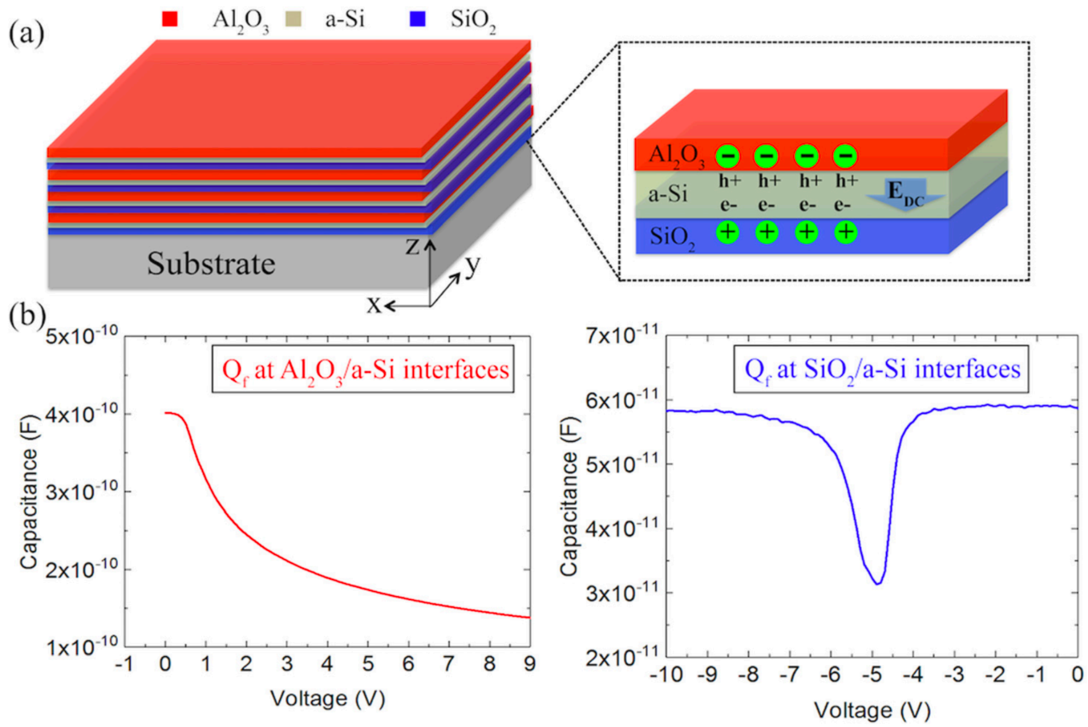


Figure 2.2: (a) The schematic of DSD metamaterials consisting of multiple periods of $Al_2O_3$/a-Si/$SiO_2$. (b) C-V curves for extraction of $Q_f$ at $Al_2O_3$/a- Si and $SiO_2$/a-Si interfaces at 10 kHz.

### 2.2.2 Engineered built-in electric field within semiconductor via asymmetrical claddings

Using the measured surface charges, we simulate both the symmetrical $SiO_2$/a-Si/$SiO_2$ and asymmetrical $Al_2O3$/a-Si/ $SiO_2$ stacks using the TCAD SILVACO tool to obtain the electric field distributions in these two cases as shown in figure 2.3. The thicknesses of a-Si and dielectrics are assigned to be 25 nm and 10 nm, respectively, and the thickness of a-Si is determined from the simulations to achieve a high internal electric field close to that of the Si's breakdown electric field. For the symmetrical case (black solid line), as expected, the $Q_f$ creates a narrow depletion region and the induced electric field

drops dramatically away from the surface. Due to the symmetry in the polarity of $Q_f$, the electric fields from left and right depletion regions exhibit the same magnitude but in opposite directions, resulting in a zero net field (blue dashed line) within the a-Si layer. On the other hand, for the asymmetrical case (red solid line), different $Q_f$ polarities on each side create a depletion region that extends into the entire a-Si layer, resulting in a constant non-zero statistic electric field ( $1x10^5$ V/ cm) inside the a-Si.

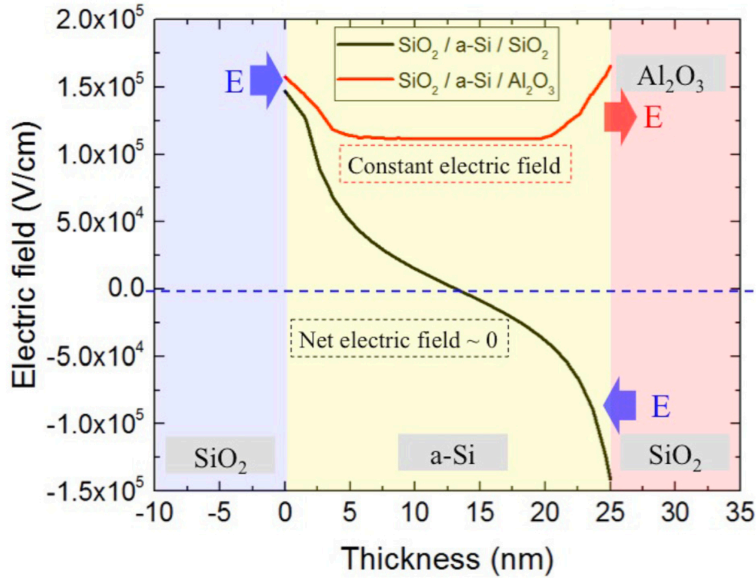


Figure 2.3: Simulated electric field within the 25 nm a-Si layer in symmetrical (black solid curve) and asymmetrical (red solid curve) DSD metamaterials. The blue dashed line shows that the net electric field is zero for the symmetrical case.

### 2.2.3 Metamaterials consisit of dielectric/semiconductor/dielectric stacks

This high field is expected to interact with a-Si's inherent $\chi^{(2)}$, which ranges from $2.3x10^{19}$ to $9.2x10^{19}$ $m^2/V^2$ at a wavelength of 800 nm to induce a prominent effective $\chi^{(2)}$ (i.e., 3.8 to 15.3 pm/V) through the EFISH effect in the asymmetrical DSD stack. To validate this approach experimentally, we fabricated four samples, with one and two

periods of asymmetrical ($Al_2O_3$ (10 nm)/a-Si (25 nm)/$SiO_2$ (10 nm)) and symmetrical ($SiO_2$ (10 nm)/a-Si (25 nm)/$SiO_2$ (10 nm)) stacks on fused silica substrates.

Regarding to the fabrication, the dielectric/a-Si/dielectric metamaterials are grown on fused silica substrates at room temperature in a high vacuum environment by magnetron sputtering. Substrates undergo thoroughly cleaning processes with acetone, isopropyl alcohol and deionized water before deposition, to prevent from inaccuracy of optical characterization due to adhesion of particles on the surfaces. Deposition of $SiO_2$, a-Si, and $Al_2O_3$ thin film is carried out by means of reactive sputtering under an argon and oxygen environment. It should be noted that the thickness of $SiO_2$ and $Al_2O_3$ layers are kept at 10 nm to make sure the films are thick enough to generate sufficient fixed charges at their respective interfaces with silicon, and the thickness of a-Si is set as 25 nm, to ensure a constantly high electric field that can penetrate through the entire layer. The gas flow rate, the type of target and deposition time are all controlled with software, therefore, one and two cycles of the DSD stack (i.e., $SiO_2$/a-Si/$SiO_2$ (symmetrical) and $Al_2O_3$/a-Si/$SiO_2$ (asymmetrical)) can be easily deposited within one-step without the need of breaking vacuum. After each layer deposition, the targets are etched for one minute in pure argon gas to remove contaminated native oxides before the ongoing layer is deposited. The deposition rate of each target and crystallization of films are characterized by means of small angle x-ray reflectivity. Sputtered layers are all confirmed to be amorphous, and the thickness and refractive index of films are measured with a Rudolph Auto EL Ellipsometer.

## 2.3 Results

The characterization of second-order nonlinearities of these DSD metamaterials is performed using the Maker fringe setup, the details of which are mentioned in supplementary materials, wherein a fs Ti-Sapphire laser at 800 nm was used as a pump with a fixed incident angle of 45 degrees. Figure 2.4(a) shows the measured second-harmonic optical power with mixed polarizations (combination of p- and s- polarized waves) generated from one and two periods of the asymmetrical nonlinear metamaterial as a function of pump power. The detected signals, as expected, scale quadratically with the pump power, verifying the fact that the detected signal comes only from the SHG effect of the thin film stacks. Figure 2.4(b) shows the generated p- and s-polarized SHG signals from one and two periods of the asymmetrical metamaterial as a function of the polarization angle of the pump field, where 0 stands for the s-polarized and 90 represents for the p-polarized fundamental beam. The result for the p-polarized SHG from two periods of the symmetrical DSD composite metamaterial is also shown for comparison (i.e., red). The curves corresponding to the symmetrical metamaterial show a relatively low signal, which is close to the background noise of our setup, indicating that no observable SHG effect occurs. This experimental result is consistent with our theoretical prediction that EFISH is negligible for the case when a-Si is cladded with the same dielectric on both interfaces. In contrast, both the p- and s-polarized SHG signals generated from asymmetrical samples are prominent. The bare fused silica substrate and single layers of a-Si, $Al_2O_3$, and $SiO_2$ separately grown on silica are all measured under the same experimental conditions as those used for the characterization of DSD metamaterials, and no observable signals were

detected. These results confirm the fact that the contribution of quadrupolar and magnetic dipoles and interfacial effects to the observed SHG signal is negligible in our case, and the prominent SHG in the asymmetrical DSD meta- material originates from bulk a-Si layers though the EFISH effect.

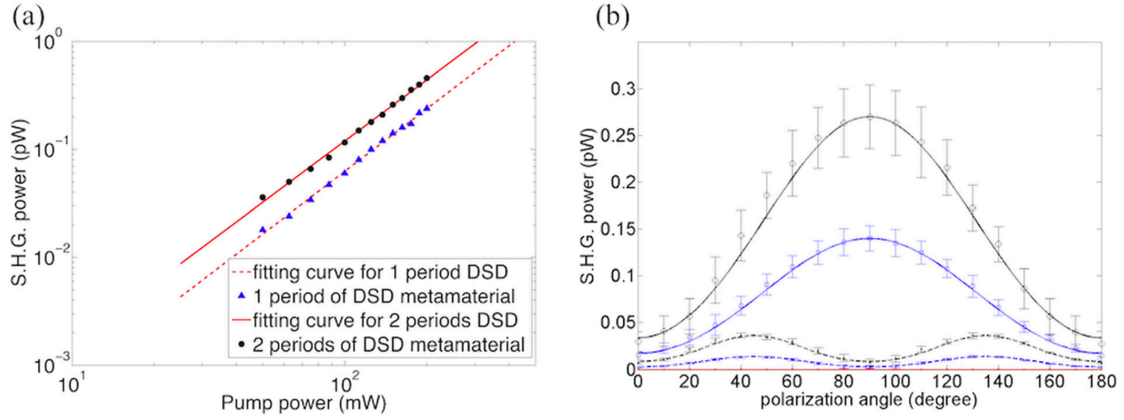


Figure 2.4: The generated (combination of p- and s-polarized) second-harmonic responses versus pump power from one (blue triangles) and two periods (black circles) of the asymmetrical DSD stack plot on a log-log scale. (b) The p- and s-polarized second-harmonic signals generated from one and two periods of the asymmetrical metamaterial (blue for one period and black for two periods of the DSD stack; solid lines for generated p- and dashed lines for generated s- polarized SHG responses) and two cycles of the symmetrical DSD stack (red) under variant polarization angles of pump light, where the average power is 150 mW with a fixed incident angle of 45 degrees.

By fitting these data and using the Maker fringe analysis (see Appendix B), we calculate all the three independent components of the $\chi^{(2)}$ tensor: $\chi^{(2)}_{zzz}$, $\chi^{(2)}_{xxz}$, and $\chi^{(2)}_{zxx}$ as represented in Table I, and the coordinate system is shown in figure 2.2(a). The value of the dominant diagonal component, $\chi^{(2)}_{zzz}$, is 2 pm/V and has the same direction as the induced built-in electric field within the a-Si layer, proving that the effective $\chi^{(2)}$ in the asymmetric metamaterial originates mostly from the EFISH effect. The small discrepancy between the expected and the measured value originates from the considered $\chi^{(2)}$ value for a-Si [44]. Also, the calculated $\chi^{(2)}$ tensors from samples with one and two periods of the stack match each other, indicating that the medium composed of more cycles of the

asymmetric DSD stack exhibits the same nonlinear properties, enabling potential applications of devices in a waveguide configuration for on-chip realization of nonlinear optical devices. The generated second-harmonic signals from the two periods of the DSD stack are only twice as large as the one generated from one period of the DSD stack, which does not obey the theoretical prediction that the generated SHG intensity scales quadratically with the interacting length. The discrepancy can be attributed to a lower transmittance in the two periods of the DSD stack due to the absorption in the a-Si layer at both wavelengths, the fundamental (i.e., 800 nm) and the second-harmonic (i.e., 400 nm) signals [45]. Considering absorption (i.e., the imaginary part of the refractive index) in the Maker fringe analysis, we predict a SHG power 1.6 times larger for the two periods of the DSD stack, within the error bars of our experiment. Small discrepancies may occur due to the actual values of the real and imaginary parts of refractive indices considered in our study. It should be noted that this loss can be significantly reduced when operated with wavelengths where a-Si is transparent.

Table 2.1: Calculated components of the effective $\chi^{(2)}$ tensors.

| Second-order nonlinear susceptibility (pm/V) | One period | Two periods |
|---|---|---|
| $\chi^{(2)}_{zzz}$ | 1.9 ± 0.4 | 2.1 ± 0.4 |
| $\chi^{(2)}_{xxz}$ | 0.4 ± 0.1 | 0.4 ± 0.1 |
| $\chi^{(2)}_{zxx}$ | 0.3 ± 0.1 | 0.3 ± 0.1 |

In the theory, the magnitude of the effective $\chi^{(2)}$ in the DSD metamaterial can be further enhanced by either increasing the magnitude of the built-in electric field or choosing

semiconductors that exhibit higher $\chi^{(2)}$. To induce a higher electric field within the a-Si layer, an efficient way is to increase the magnitude of the $Q_f$ density at dielectric/semiconductor interfaces by treating as-deposited samples with an annealing process. The heating treatment offers sufficient energy for inactive charge centers to contribute more to the separation of ions and free carriers, thus increasing the density of $Q_f$. To understand the influence of annealing treatment on the density of $Q_f$, we fabricated test samples and performed C-V measurements on $SiO_2$/a-Si and $Al_2O_3$/a-Si interfaces shown in figure 2.5(a) and 2.5(b) for the as-deposited samples and the samples annealed at different temperatures (i.e., 200, 300, and 400 C) for 15 min. As the plots show, the flat-band voltage, $V_{fb}$, for both cases shifts away from the work function difference between a-Si and the aluminum electrodes, indicating that the magnitude of $Q_f$ in both $SiO_2$ (positive) and $Al_2O_3$ (negative) . AG Associates Heat Pulse 610 is used for the rapid thermal annealing (RTA) processes. The as-deposited samples are loaded into a sealed chamber in a $H_2/N_2$ environment, while the flow rate of $H_2$ and $N_2$ are set both to be 100 sccm. Then the temperature is risen up to the assigned point (200, 300 and 400$^o$C) in 10 seconds, keeping for 15 minutes, and naturally cooling down to room temperature.

To validate the enhanced magnitude of the effective $\chi^{(2)}_{zzz}$, we carried out experiments on analyzing the p- polarized SHG signals from samples with one and two periods of the DSD stack annealed under different conditions as shown in figure 2.5(c) and 2.5(d), respectively. In both cases, the samples annealed at 400$^o$C (blue circle) show the highest second-harmonic intensity, which matches the prediction from the results of C-V measurement. In figure 2.6, we summarize the calculated $Q_f$ at $SiO_2$/a-Si (in blue squares) and $Al_2O_3$/a-Si (in red squares) interfaces and the extracted values of the effective $\chi^{(2)}_{zzz}$

from one (brown circle line) and two periods (green square line) of metamaterials for samples with different annealing treatments. The magnitude of both positive and negative $Q_f$ generated at either top or bottom interfaces increases with the annealing process at higher temperature, and the calculated effective $\chi^{(2)}_{zzz}$ in one period and two periods of the asymmetric annealed metamaterial also shows the same trend. The highest effective $\chi^{(2)}_{zzz}$ is calculated to be 8.5pm/V for the sample treated by the 400°C annealing process, which shows 4 times enhancement than that obtained from the as-deposited sample (i.e., 2 pm/V).

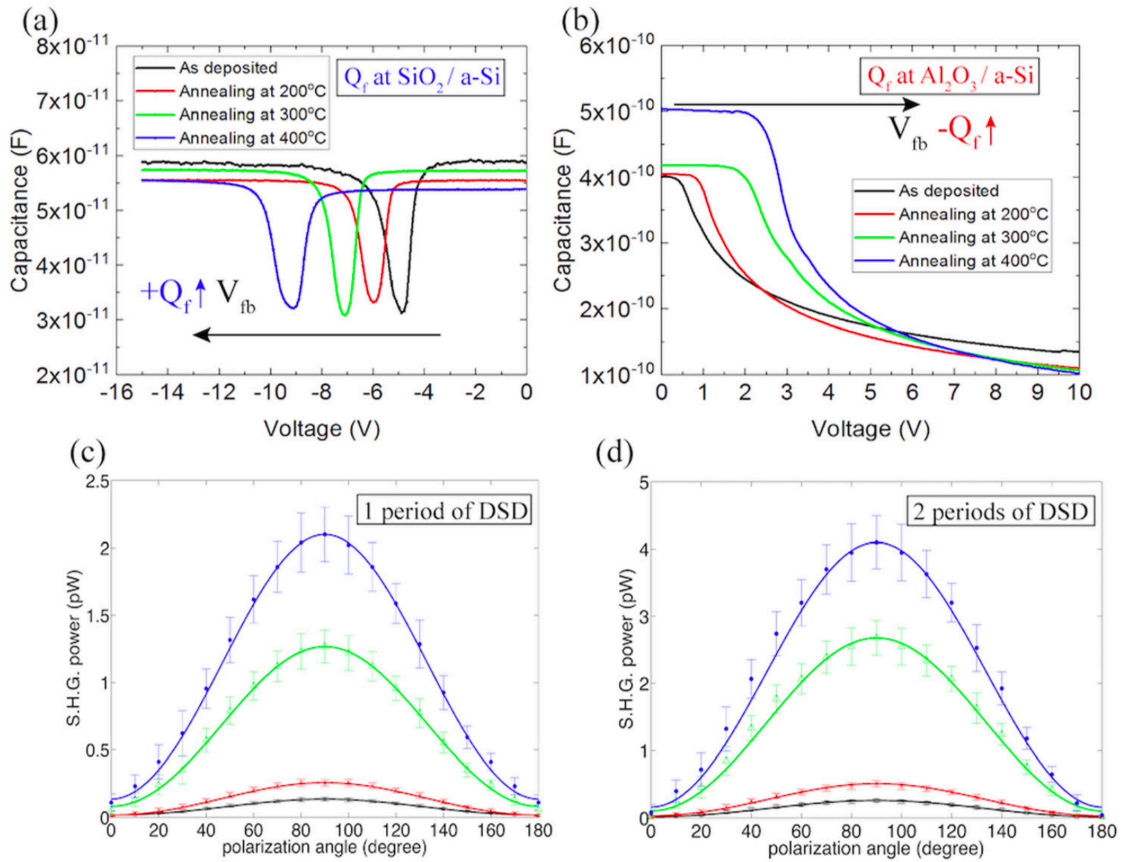


Figure 2.5: C-V measurements on (a) $SiO_2$/a-Si and (b) $Al_2O_3$/a-Si interfaces for as-deposited (black), 200°C (red), 300°C (green), and 400°C (blue) annealed samples. The generated p- polarized SHG signals from (c) one and (d) two periods of asymmetrical DSD metamaterials at different temperatures of annealing treatment with variant polarization angles of the incident laser.

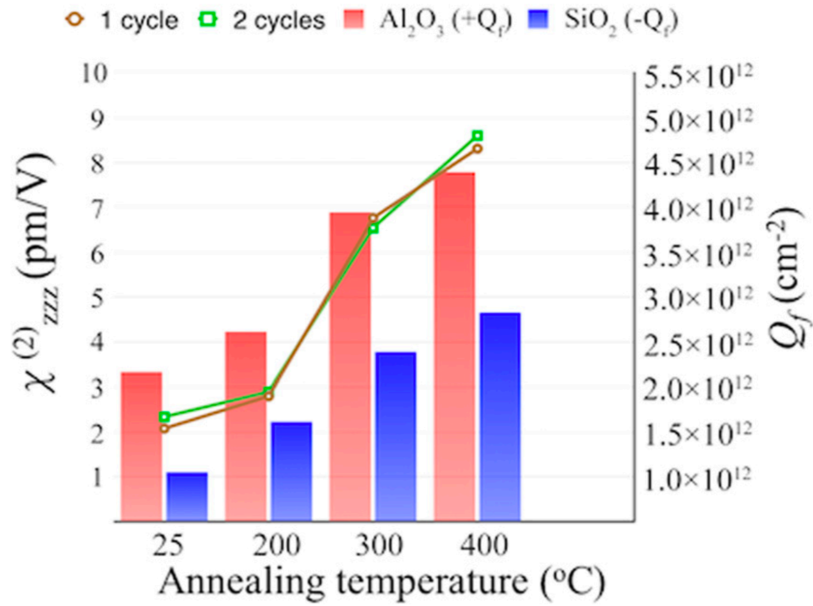


Figure 2.6: The calculated $Q_f$ in $SiO_2$/Si (blue boxes) and $Al_2O_3$/Si (red boxes) interfaces and the extracted effective $\chi^{(2)}_{zzz}$ in one (brown circles) and two (green squares) periods of asymmetrical metamaterials.

The nonlinearity of the DSD metamaterials has been experimentally demonstrated with the free-space measurement. In figure 2.7(a), a lumerical FDTD simulation shows the fundamental guiding mode for DSD metamaterials at the wavelength of 1.55 um, where silicon is transparent, and the fabricated ring resonator structure using DSD metamaterials is shown in figure 2.7 (b). The cross-section view of the DSD metamaterial deposited using magnetron sputter is shown in figure 2.8 imaged with STEM.

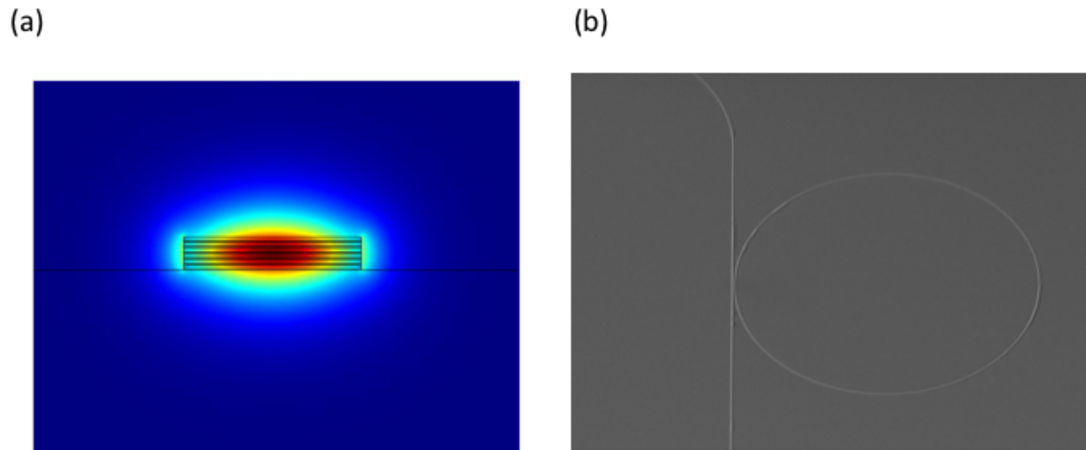


Figure 2.7 (a) Calculated mode for DSD metamaterials at the wavelength of 1.55 micro-meters. (b) Ring resonator waveguide structure fabricated using DSD metamaterials.

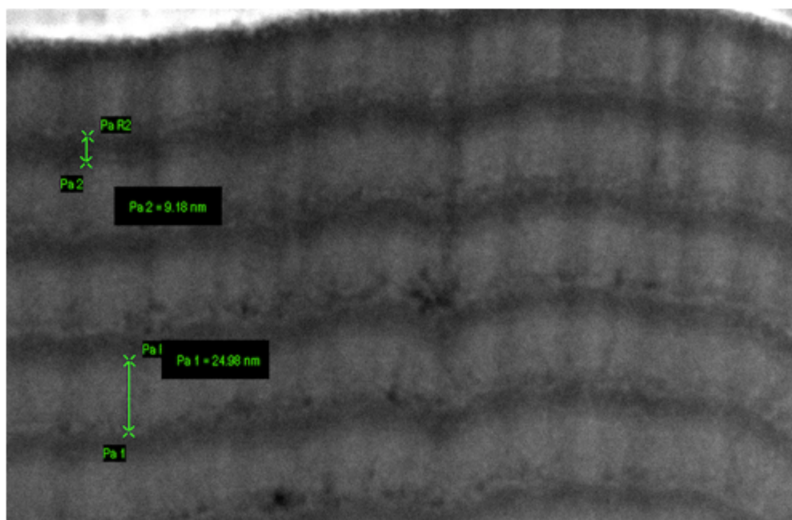


Figure 2.8 STEM figures of DSD metamaterials deposited by a magnetron sputter machine.

## 2.4 Discussion

We experimentally proved that the effective $\chi^{(2)}$ can be increased with post annealing process from activating more charges at the dielectric/semiconductor interfaces. We propose to further optimize the annealing conditions to obtain higher value of effective $\chi^{(2)}$ in DSD metamaterials. It is also possible to enhance the SHG by increasing the number of periods of the DSD metamaterial. Effectively, the interaction length for free space wave mixing will increase since it is proportional to $NL_{sem}$, where N is the number of periods and $L_{sem}$ is the thickness of the semiconductor layer. Once the total thickness reach hundreds of nanometer or even a few microns, it is also possible to process the metamaterial and fabricate waveguides for efficient nonlinear processing on-chip. Compared to the distribution of effective $\chi^{(2)}$ in dielectric clad silicon waveguide, such waveguide made from multilayered DSD metamaterials exhibit the induced effective $\chi^{(2)}$ through the entire bulk volume of the waveguide, thus maximizing overlap with the propagating guided mode. The efficient exploitation of fixed charge induced effective nonlinearities makes the conceptual DSD metamaterials a perfect candidate for second-harmonic generation in waveguide configurations.

## 2.5 Conclusion

In summary, we have theoretically and experimentally demonstrated an approach to engineer CMOS-compatible nonlinear metamaterials by exploiting the generated fixed charges at dielectric/semiconductor interfaces. Asymmetrical DSD metamaterials exhibit an average effective $\chi^{(2)}_{zzz}$ of 2 pm/V in the bulk via exploiting the charges existing at interfaces, and the magnitude can be further enhanced up to 8.5 pm/V with proper thermal annealing treatment. In the theory, larger effective $\chi^{(2)}$ can be achieved by either increasing $Q_f$ with optimization of fabrication processes or replacing the a-Si with other semiconductor candidates exhibiting both larger break down fields and larger $\chi^{(3)}$. Since the composite films are all CMOS-compatible and grown by magnetron sputtering at room temperature, the pro- posed formation of nonlinear metamaterials can be customized with various dielectric and semiconductor materials for variant applications.

We have also demonstrated that if the number of periods is increased, the effective $\chi^{(2)}$ is the same in the multiple semiconductor layers composed of the DSD metamaterials. Indeed, this feature enables using such metamaterials as waveguide cores provided that large optical mode-metamaterials overlap, which offers efficient nonlinear behaviors exploiting the induced effective $\chi^{(2)}$. With further optimization of their optical linear and nonlinear properties, the demonstrated DSD metamaterials exhibiting large effective second-order optical nonlinearities can be fabricated into waveguides for efficient on-chip devices such as modulators, nonlinear switches, and wavemixers.

## Acknowledgements

This chapter contains material partly from “Synthesis of second-order nonlinearities in dielectric-semiconductor- dielectric metamaterials," published at Applied Physics Letters drafted by Hung-Hsi Lin, Mu-Han Yang, Rajat Sharma, Matthew Puckett, Christian Wurm, Sergio Montoya, Felipe Vallini, Eric Fullerton and Yeshaiahu Fainman. The dissertation author was the first investigator and author of this paper.

# Chapter 3

# Metamaterials with Engineered Tuanable Optical Nonlinearities

Another idea for synthesizing high second-order nonlinear optical susceptibility ($\chi^{(2)}$) in metamaterials can be achieved via deposition of layered materials with dissimilar work functions. Specifically, we propose to explore metal/semiconductor/metal (MSM) metamaterial using amorphous silicon clad with different metal layers. Metals with dissimilar work functions on either side of a semiconductor create a non-zero net electric field across the semiconductor layer at thermal equilibrium. Consequently, the built-in electric field in a semiconductor with large third-order nonlinear susceptibility will result in an enhanced, effective second-order nonlinear susceptibility. This composite effect can again be studied via measuring experimental SHG with the assistance of Maker fringes analysis.

## 3.1 Background

The ability to engineer metamaterials with tunable nonlinear optical properties is crucial for nonlinear optics. Traditionally, metals have been employed to enhance nonlinear optical interactions through field localization. Here, inspired by the electronic properties of materials, we introduce and demonstrate experimentally an asymmetric metal-semiconductor-metal metamaterial that exhibits a large and electronically tunable effective second-order optical susceptibility. The induced $\chi^{(2)}$ originates from the interaction

between the third-order optical susceptibility of the semiconductor with the engineered internal electric field resulting from the two metals possessing dissimilar work function at its interfaces. We demonstrate a five times larger second-harmonic intensity from the MSM metamaterial, compared to contributions from its constituents with electrically tunable nonlinear coefficient ranging from 2.8 to 15.6 pm/V. Spatial patterning of one of the metals on the semiconductor demonstrates tunable nonlinear diffraction, paving the way for all-optical spatial signal processing with space- invariant and -variant nonlinear impulse response.

## 3.2 Materials and Methods

### 3.2.1 Junction generated at metal/semiconductor interfaces

As metal and a-Si semiconductor are brought into contact, metal which has lower work function causes diffusion of electrons into a-Si until thermal equilibrium is reached and the Fermi levels, $E_F$ of a-Si and metal align. The charge redistribution results in a built-in or diffusive potential, and creates a built-in static electric field close to the metal- a-Si interface, bending the bands of a-Si downwards. Once the semiconductor is clad with the metals with different work functions, a static electric field might be generated within the semiconductor layer resulting from the difference in the Fermi levels of the two metals on either side of a-Si.

### 3.2.2 Engineered built-in electric field within semiconductor via asymmetrical metal claddings

The principle of the proposed MSM nonlinear optical metamaterial is schematically shown in figure 3.1(a), where thin layers of a-Si are clad with metal A and metal B which have different work functions. Figure 3.1(b) shows the band diagram of a-Si without contacting with metals. In our example, we consider the work functions of metals A and B (i.e., $\phi_A$ and $\phi_B$) to be smaller and larger than that of intrinsic a-Si (i.e., 4.67 e.V.), respectively. Figure 3.1(c) shows an example of the reduced band diagram in symmetrical MSM structure, where metal A is used to clad the a-Si layer on both interfaces, resulting in two depletion regions with built-in electric fields equal in magnitudes but pointing in opposite directions at each interface. Consequently, the net electric field, $E_{DC}$, across the a-Si layer is zero. However, once we replace metal A with metal B with a larger work function on one side of the a-Si layer, the heterostructure becomes asymmetric with the bands bent upwards close to the metal B-a-Si interface, resulting in an asymmetric built-in potential within the a-Si layer (see figure 3.1(d)), and consequently a non-zero $E_{DC}$ across the layer of a-Si. The difference in the metals' work functions and that of a-Si determines the depletion width and hence the magnitude and penetration depth of the induced electric field which can range from tens to hundreds of nanometers. With an appropriate choice of the two metals, a high static electric field can be induced in the a-Si layer, leading to a high effective second-order nonlinear optical coefficient, $\chi^{(2)}$ within a-Si, via the EFISH effect.

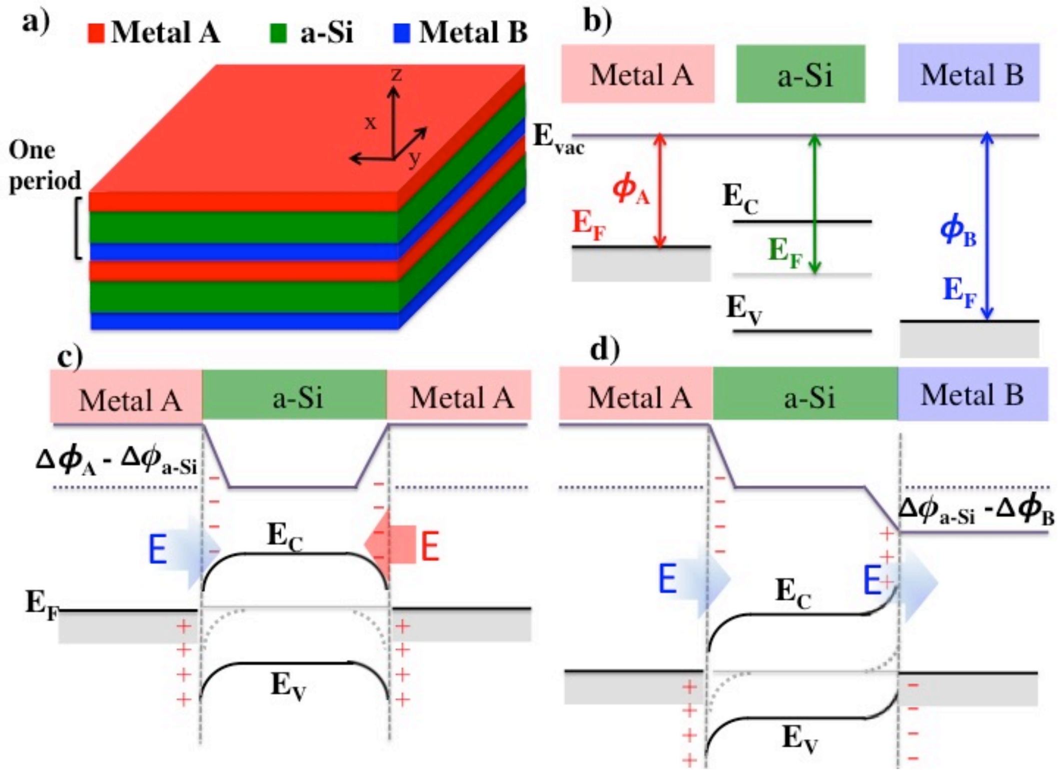


Figure 3.1: (a) The schematic of a MSM metamaterial consisting of a-Si clad with two different metals, metal A and metal B. (b) The reduced band diagram of a-Si, metal A and metal B without intimate contact. (c) The reduced band diagram of symmetrical and (d) asymmetrical MSM structures under equilibrium with intimate contact.

### 3.2.3 Metamaterials consisit of metal/semiconductor/metal stacks

The basic principle of the proposed MSM nonlinear optical metamaterial and the SEM image of the fabricated structure are shown in figure 3.2 (a), where a thin layer of a-Si is clad with Al and Ni which have respectively smaller and larger work function (i.e., Al with 4.08 eV and Ni with 5.01 eV) [46,47], compared to the work function of a-Si (i.e., 4.67 eV). Consequently, a static electric field is generated within the bulk of the a-Si semiconductor layer. The band diagram of the MSM structure is included as an insert in figure 3.2 (b) showing a-Si's energy band gap $E_g$, Fermi level $E_F$, valence and conduction

bands energies $E_V$ and $E_C$ respectively. $\varphi_{Al}$ and $\varphi_{Ni}$, are the work function of Al and Ni respectively.

We use TCAD Silvaco simulation tool to study the magnitudes and spatial distributions of the built-in electric fields inside the MSM metamaterial structures consisting of a 25 nm thick a-Si layer clad with 5 nm thick Al and Ni thin films (see figure 3.2(b)). As expected, the net electric field in the case of the MSM metamaterial is non-zero corresponding to an average DC electric field of $3.5 \times 10^5$ V/cm. Since the a-Si layer exhibits a large third-order nonlinear susceptibility, $\chi^{(3)}$ ($\sim 2.3 \times 10^{-19}$ to $9.2 \times 10^{-19}$ $m^2/V^2$) [40,44] the induced DC electric field is expected to result in a high effective $\chi^{(2)} = 3\chi^{(3)}E_{DC}$, ranging from 10 to 40 pm/V.

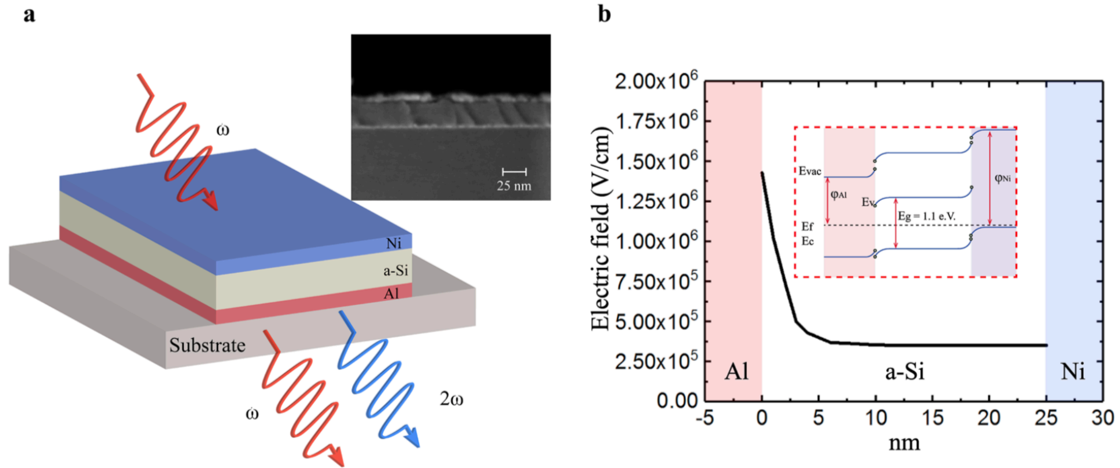


Figure 3.2: (a) Schematic and SEM image of a 5 nm Ni/25 nm a-Si/5 nm Al MSM metamaterial for second-harmonic generation process. (b) Reduced band diagram and the simulated distribution of built-in electric field for the Ni/a-Si/Al metamaterial.

## 3.3 Results

Besides investigation of the nonlinearities in the MSM stack, the transmission is also a crucial optical property that needs to be studied. First we calculate the transmission of both TE- and TM- polarization light in a MSM structure (Al (5nm) / a-Si (25nm) / Ni (5nm)) by inputting real and imaginary part of refractive indices for each constituent material, while the wavelength of incident beam is set at 800 and 400 nm under variant incident angles (see figure 3.3). These properties are critical for calculating the effective components of $\chi^{(2)}$ tensor. The low transmission is due to the inherent optical losses of metals and a-Si at optical visible frequencies, and it can be improved by further reducing the thickness of metal films. We believe that the transmission of the MSM stack could be much higher than the prediction made here with optimization of the thickness. Also, the other part of optical loss comes from the absorption of a-Si at both frequencies.

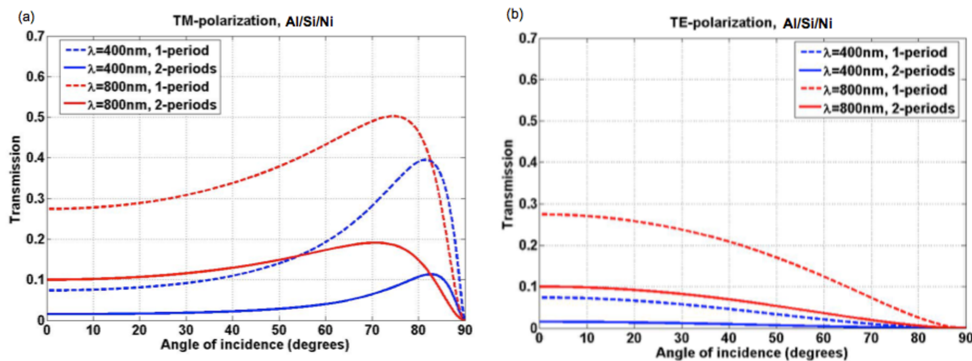


Figure 3.3: Transmission of TM-(a) and TE-(b) polarization of one and two periods of Al / a-Si / Ni stack under variant incident angles with wavelength at 400 and 800 nm.

For an experimental validation of our hypothesis, we designed and fabricated the MSM metamaterial on fused silica substrates using magnetron sputter deposition at room

temperature. e metal/a-Si/metal metamaterials are grown at room temperature in an ultra-high vacuum environment by magnetron sputtering. Samples are deposited from Si-undoped (99.999%), Pt (99.95%), Ni (99.95%) and Al (99.95%) pure elemental targets onto fused silica substrates under an Ar pressure of 3 mTorr. Substrates undergo a thorough cleaning processes with Acetone, Isopropyl alcohol and deionized water before deposition, to prevent any inaccuracy in the optical characterization due to adhesion of particles on the surfaces. The thickness and refractive index of films are measured with the Rudolph Auto EL Ellipsometer. The deposition rate of each target and crystallization of films are characterized by means of small angle x-ray reflectivity (XRR) with a Bruker D8 Discover x-ray diffractometer. The XRR measurements confirm the fact that all sputtered films are amorphous.

We then experimentally estimate the induced $\chi^{(2)}$ coefficients in a-Si layer by measuring the generated SHG intensity and subsequently using the revised Maker fringes analysis described in details in the Appendix C. First, to ensure that the detected signal is generated via the second-order nonlinear process from the bulk of deposited a-Si semiconductor, we analyze the measured signals as a function of the input pump power for both the MSM metamaterial as well as single layers of the cladding metals Al and Ni on fused silica substrates (see figure 3.4 (a)). The measured intensities from all samples are confirmed, as expected, to be quadratically dependent on the pump power, illustrating the fact that the detected signals indeed originate from the second-order nonlinear responses. The a-Si film and the substrate are also confirmed to provide zero SHG signal as a result of their null $\chi^{(2)}$. We then apply Marker fringes method to characterize the polarization dependence of the SHG for extracting the $\chi^{(2)}$ tensor coefficients. The measured p- and s-

polarized second-harmonic responses as a function of the polarization angle of the input pump are shown, for all the three cases, in figure 3.4(b) and (c), respectively. For both polarizations, the SHG intensities from the MSM are clearly much larger than that generated from a combination of Al and Ni layers on fused silica substrates, implying that, as expected, the second-order nonlinear response is dominated by the a-Si layer due to the existence of the non-zero built-in electric field.

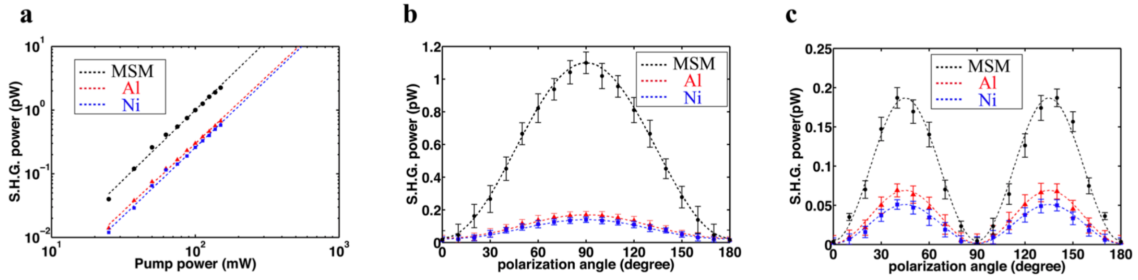


Figure 3.4: (a) Log-log plot of measured SHG signal versus pump power for a single layer of Al (red triangles), Ni (blue squares) thin film and MSM metamaterial (black circles) grown on silica substrates for a fixed pump-beam incident angle of 45°. (b) Generated p-polarized and (c) s-polarized SHG intensity versus polarization angle for a 100 mW pump.

To further confirm our theory, we fabricated one more MSM metamaterial sample, replacing the top clad of Ni with platinum (Pt). Pt, just like Ni, has a larger work function (i.e., 5.65 e.V.) [46] than that of a-Si, and hence is expected to result in a non-zero built-in electric field in the a-Si layer in combination with the bottom clad of Al. The intensities of measured SHG from the Pt/a-Si/Al composition are measured and compared with the previous samples (i.e, Ni/a-Si/Al), as shown in figure 3.5, under the same experimental conditions. The SHG signal from the bottom Al cladding layer (red boxes) is fixed in all cases, and the signals from the top metal cladding films are measured individually and represented by blue boxes. The differences between the measured signals from the MSM

metamaterials and their metallic constituents correspond to the contribution from a-Si layer (yellow boxes). It is apparent from figure 3.5 that the SHG signal in both MSM samples are significantly larger than the contributions from individual responses of their respective constituents. The generated second-harmonic field intensity can in fact be five times larger than the SHG signals from the respective constituents (e.g., individual Al, Ni and Pt metal films). Furthermore, it also confirms our hypothesis, the contribution from the a-Si layer is found to be proportional to the difference of work functions between bottom and top metals, i.e., proportional to the built-in electric field. It can be envisioned that similar to the work demonstrated in this study, MSM metamaterials can, in the future, be custom-synthesized by choosing an appropriate combination of clad metals and semiconductor layer.

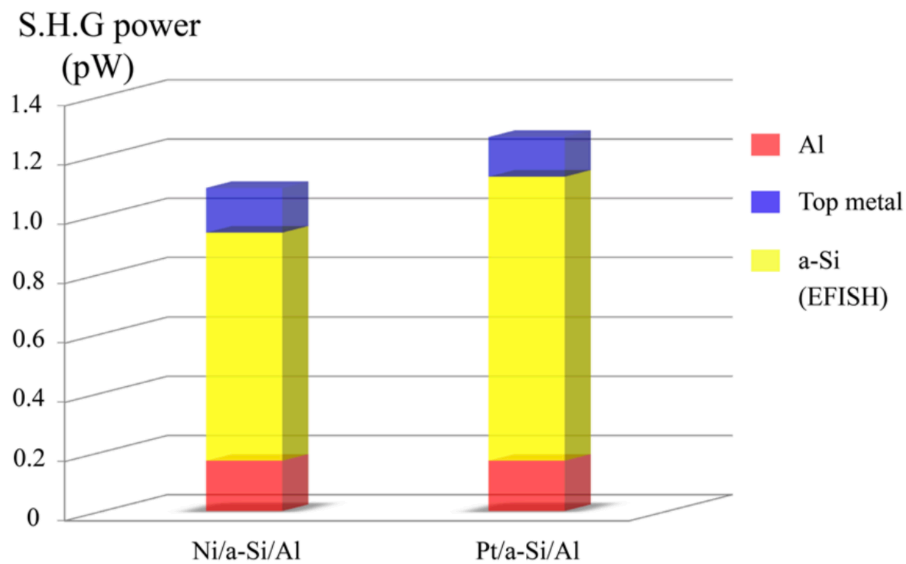


Figure 3.5: Measured SHG intensities from the Ni/a-Si/Al (left) and Pt/a-Si/Al (right) MSM metamaterials and their constituents. The red boxes show the SHG from a single layer of Al film, and the blue boxes show the SHG from top cladding metal films. The difference between the total measured SHG intensities from the MSM metamaterials and their components is then assumed to be from the bulk of the a-Si (yellow) layer via EFISH effect.

Additionally, the components of $\chi^{(2)}$ tensor in these MSM metamaterials are also estimated. We consider the thin MSM structures as a uniform isotropic effective medium [48], and then calculate all the induced $\chi^{(2)}$ tensor components using the measured p- and s-polarized SHG signals for each of the MSM metamaterial samples (Appendix C). It should be noted that for more accurate theoretical estimate of the SHG via EFISH effect in our metamaterials one could consider optical field localization effects on each metal-semiconductor interface. The measured results are summarized in the Table 3.1. Comparing the magnitude of all non-zero tensor components, it is apparent that the all-normal tensor component, $\chi^{(2)}_{zzz}$, which is parallel to the direction of the built-in electric field, is dominating, proving conclusively that the additional contribution to the second-order nonlinear response of an asymmetrical MSM metamaterial is truly a result of the engineered electronic band structure in the bulk of the a-Si layer.

Table 3.1: Calculated components of the effective $\chi^{(2)}$ tensors in MSM metamaterials

| Second-order nonlinear susceptibility (pm/V) | Ni/a-Si/Al | Pt/a-Si/Al |
|---|---|---|
| $\chi^{(2)}_{zzz}$ | 7.2 ± 1.5 | 8.9 ± 1.6 |
| $\chi^{(2)}_{xxz}$ | 1.9 ± 0.5 | 2.2 ± 0.8 |
| $\chi^{(2)}_{zxx}$ | 2.3 ± 0.8 | 2.3 ± 0.7 |

Since our experiments were carried out using optical fields with photon energies larger than bandgap of a-Si, we need to consider the effect of generated free-carriers that may affect the magnitude of the induced effective $\chi^{(2)}$. The pump generated photocarriers could lower the Schottky barriers between the semiconductor and metals, and cause a reduction in the induced built-in electric field. To estimate the strength of this effect, we measured and analyzed the I-V behaviors of the MSM stack (see Appendix C). These experiments show that the built-in barrier height within the a-Si layer, under illumination with an average power of 100 mW (i.e., the power used in our experiments on SHG), will be reduced by 15% compared to its value under no illumination. is reduction, resulting from the image-force effect as a consequence of the generated photocurrent, however results in a reduction of the built in electric field by no more than 10% for the average pump-powers employed in this study. Therefore, we conclude that the pump-generated photocarriers have a relatively minor effect on the measured effective $\chi^{(2)}$. It should be noted that the reported measured values of effective $\chi^{(2)}$ may increase by avoiding photocarrier generation using pump photon energies smaller than the bandgap of a-Si (e.g., 1550 nm range).

In addition to their passive optical behavior, MSM metamaterials also enable the active control of their second-order nonlinear optical response by applying an external electric field using the constituent metals as electrodes. To illustrate this, experiments were carried out on a MSM metamaterial sample fabricated with a thicker a-Si layer of 50 nm, since the built-in electric field in the 25 nm thick a-Si layer is already close to the breakdown limit. The schematic of this active MSM structure is shown in figure 3.6(a). An external DC voltage is applied across the a-Si layer, and the generated SHG signal is

measured for bias voltages ranging from −2.5 V to +1.5 V. Figure 3.6(b), shows the measured SHG intensity varying quadratically as a function of the applied field, which is expected for a linear change in the second-order nonlinear susceptibility coefficient as a function of the applied bias. A positive voltage increases the generated SHG signal by inducing more asymmetry in band structure of the a-Si layer, until the built-in electric field reaches the breakdown limit, which in our case occurs at +1.5 V. For negative voltages, we observe a reduction in the SHG signal as a result of the reduction in the built-in electric field. At the at-band voltage, which is negative in this case, the electric field inside the semiconductor is completely eliminated, removing any of its contribution to the observed second-harmonic response. It should be noted, that even at this voltage we observed a finite, non-zero, SHG signal, due to the two metal films. However, this is not the voltage corresponding to the absolute minimum observed second-harmonic signal. is, in fact, is achieved at a voltage of −0.75 V, where the generated second-harmonic field intensities from a-Si and the metals are out of phase and completely cancel each other. The measured intensity, however, still does not reach a zero value, which is attributed to the fact that the non-diagonal components of $\chi^{(2)}$ tensor still remain non-zero and result in a finite SHG signal. As the magnitude of the voltage applied is increased further, the SHG signal increases again until the breakdown field is reached, which occurs at −2.5 V. It is noteworthy that the induced effective dipoles in a MSM metamaterial under negative and positive fields should exhibit opposite directions even though the measured SHG signal shows the same magnitude. The minimum and maximum values of the measured SHG intensity are then used to determine that a wide tunable range of 2.8 to 15.6 pm/V is achievable for of the effective $\chi^{(2)}{}_{zzz}$ tensor in this MSM metamaterial.

In addition to these results, we also explore the possibility of spatially patterning one of the metal layers in our MSM structure, to electrically control the local spatial strength of the induced second-order nonlinearity. For simplicity, we pattern one of the electrodes into a periodic structure (i.e., grating), but more complex spatial structures with multiple control lines are indeed possible. A schematic diagram and the corresponding SEM image of the fabricated device are shown in figure 3.6(c). The Ni film is patterned with a periodicity of 10 μm and a duty cycle of 0.5. We fabricate a total of 40 periods to ensure that the size of this pattern is larger than the spot size of our laser pump beam. Such a device exhibits alternating regions with different magnitudes of $\chi^{(2)}$. When a pump beam at frequency $\omega$ is incident on such a device, the generated second harmonic field will produce diffraction orders. Figure 4d shows the detected SHG signal exhibiting both 0th and symmetrical ± 1st diffraction orders. Furthermore, when an external voltage is applied across this patterned MSM structure, such that the applied electrical field is in phase (i.e., polarity) with the internal field, we obtain an enhanced diffraction efficiency (see figure 3.6(d), red squares) whereas when the polarity is reversed, we obtain a corresponding reduction in the diffraction efficiency (see figure 3.6(d), blue triangles) of the SHG signals. The tunability of the demonstrated spatially patterned second-harmonic response may enable novel optical signal processing applications with tailored space-invariant as well as space-variant nonlinear spatial impulse response.

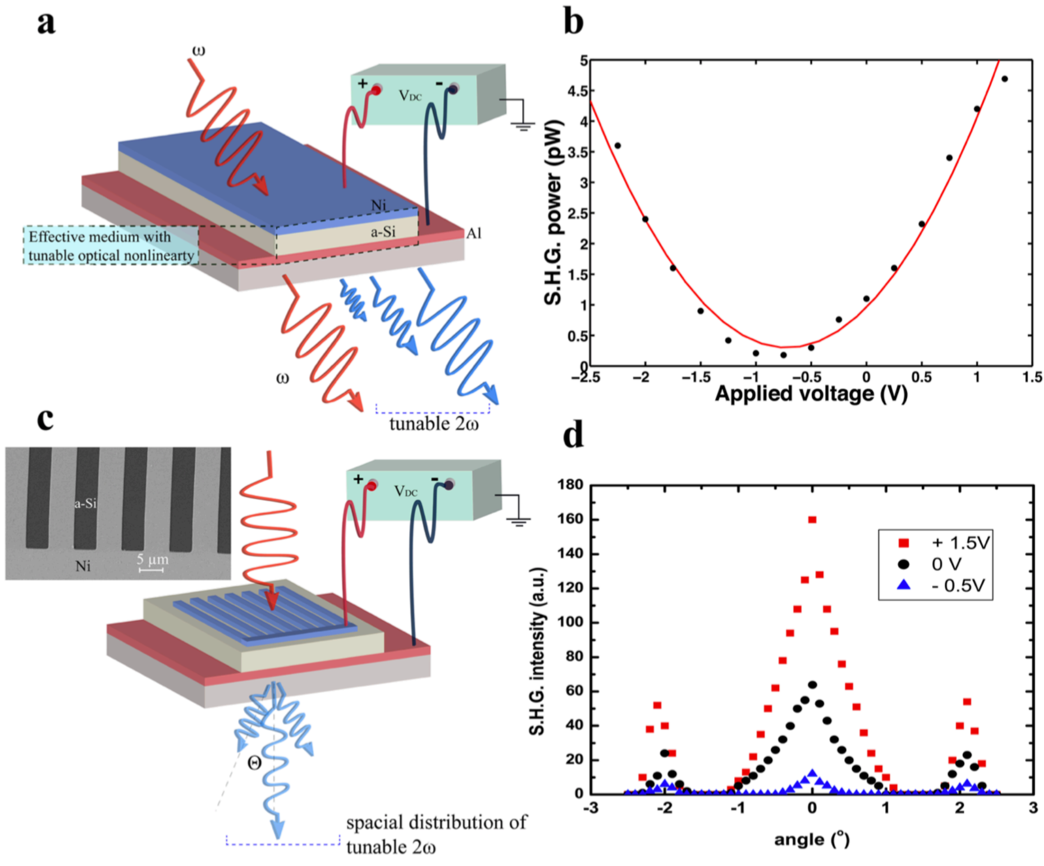


Figure 3.6: (a) Schematic of an active MSM metamaterial. (b) Measured SHG intensity under variant DC voltage (dots), and the red fitting curve showing the quadratic dependency. (c) Schematic representing the design for creating spatial nonlinear responses, and the top-view SEM image of the fabricated metal grating. (d) SHG intensity from the patterned MSM structure detected under different angles and external electrical biases.

## 3.4 Discussion

To increase the tunability of the MSM metamaterial, the future works can be replacing a-Si with other semiconductors pursing higher breakdown electric field such as SiC towards a higher amplitude tuning range [50]. With the capability of tuning the amplitude of the SHG signal the concept of MSM metamaterials exhibit a great potential for many applications such as optical switching for free-space optical communication

systems. We could focus on developing composition of materials and optimizing the fabrication processes to create a MSM stack which exhibit high tunability with low power consumption, i.e., higher built-in electric field.

## 3.5 Conclusion

Asymmetrical metal-semiconductor-metal (MSM) electronic metamaterials exhibiting a prominent and tunable effective second-order nonlinear optical susceptibilities $\chi^{(2)}$ are introduced and experimentally validated. It is conclusively shown that a large induced $\chi^{(2)}$ originates from the interaction between the bulk third-order nonlinear optical susceptibility of the semiconductor layer, $\chi^{(3)}$ with the engineered non-zero net internal electric field created by the electron transport on its interfaces with metals possessing dissimilar work functions. The MSM structures, consisting of CMOS compatible a-Si layer clad with Al-Ni and Al-Pt, are shown to generate as much as five times larger second-harmonic field intensity compared to the contribution from its constituents. The non- linear response of MSMs, proportional to the difference in the work functions of the cladding metals, is shown to be actively controlled by external electric field resulting in tunable effective $\chi^{(2)}_{zzz}$ tensor component ranging from 2.8 to 15.6 pm/V, making it suitable for on-chip optical switching and modulation. Further enhancement in the effective $\chi^{(2)}$ of the MSM metamaterials can be achieved by using a semiconductor possessing a larger $\chi^{(3)}$,with a larger breakdown voltage, and/or by improving the quality of a-Si fabrication process to increase its breakdown voltage. Moreover, by spatial patterning one of the metal layers on the interface with a-Si and varying the externally applied electric field, a tunable nonlinear diffraction effect is demonstrated, making the MSM metamaterial suitable for all-optical

spatial signal processing with tailored space invariant as well as space variant nonlinear spatial impulse response.

## Acknowledgments

This chapter contains material from “Electronic Metamaterials with Tunable Second-order Optical Nonlinearities” published at Scientific Reports in 2017 drafted by Hung-Hsi Lin, Felipe Vallini, Mu-Han Yang, Rajat Sharma, Matthew Puckett, Christian Wurm, Sergio Montoya, Eric Fullerton and Yeshaiahu Fainman. The dissertation author was the first investigator and author of this paper.

# CHAPTER 4

# SILICON-RICH NITRIDE FOR NONLINEAR OPTICAL PROCESSES

Silicon nitride ($SiN_x$) is an amorphous material, and is not expected to exhibit any second-order nonlinearity due to the amorphous nature. In free space measurements, however, silicon nitride thin films have been proved to exhibit second-harmonic generation arising from its bulk nonlinearities. But only an extremely small $\chi^{(2)}$ coefficient has been measured in an integrated platform to date, and this was attributed to interface nonlinearities [17]. If $SiN_x$ is to become a feasible replacement for silicon, it will be necessary for it to exhibit a strong electro-optic and nonlinear wave mixing effects in a waveguide configuration than what has been shown until now. In this chapter, we will introduce the non-zero $\chi^{(2)}$ in stoichiometry silicon nitride and also the enhanced $\chi^{(2)}$ in silicon-rich nitride films that have great potential as replacement for silicon in Pockels effect based modulator application.

## 4.1 BACKGROUND

In past few years, silicon nitride becomes a competing material platform, which exhibit the benefits of boasting a wider transparency window, no two-photon absorption, and an improved ease and flexibility of fabrication [50–54]. In this chapter, we report on the first experimental measurement of a bulk second-order susceptibility in silicon nitride

shown through both thin film free-space measurements and on-chip, phase-matched second-harmonic generation in waveguide configuration.

## 4.2 Materials and Methods

Here we will report the first experimental measurement of a bulk second-order susceptibility in plasma enhanced chemical vapor deposition (PECVD) deposited silicon nitride shown through both thin film free-space measurements and on-chip, phase-matched second-harmonic generation [21]. In the latter case, phase-matching is achieved through dispersion engineering of the waveguides' supported modes, and the powers contained at the second-harmonic wavelengths are used to determine the waveguides' second-order nonlinear coefficients. And then the enhanced second-order nonlinearity, by introducing more silicon contents in silicon nitride thin films will be introduced which is demonstrated experimentally in free using Maker fringes technique.

### 4.2.1 Second-order nonlinearity of silicon nitride measured in free-space

To measure the second-order nonlinear optical susceptibility, the free-space SHG experiments on $SiN_x$ thin-films was carrired out, while the films are deposited using PECVD. Film thicknesses ranging from 100-500 nm were deposited on fused silica substrates and SHG was carried out using a Maker-fringes setup wherein a fs Ti-Sapphire laser at 800 nm was used as a pump, which is shown schematically in figure 4.1(a). Figure 4.1 (b) shows the obtained second-harmonic signal as a function of input polarization for the case of 200 and 500 nm thick $SiN_x$. Then the p- and s- polarized plots are employed fto fit with a revised maker-fringes analysis for the extraction of two different components of

the $\chi^{(2)}$ tensor, which is shown in Table 4.1. These measured results are closed to the values reported from T. Ning et al., demonstrating the fact that decent magnitude of $\chi^{(2)}$ does exist in the bulk of silicon nitride thin films, it is not barely an interfacial effect.

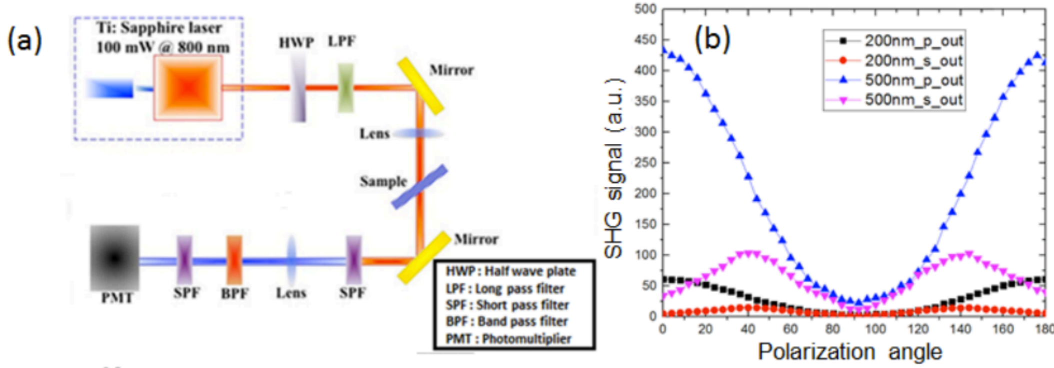


Figure 4.1: (a) Schematic of Maker fringes setup. (b) Variation of the second-harmonic signal for 200 and 500 nm thick $SiN_x$ as a function of polarization angle for the two cases of s- and p- polarized input pump.

Table 4.1: Calculated components of the effective $\chi^{(2)}$ tensors in silicon nitride with variant thickness.

| Second-order nonlinear susceptibility (pm/V) | 100 nm | 200 nm | 500 nm |
|---|---|---|---|
| $\chi^{(2)}_{zzz}$ | 2.08 ± 0.34 | 1.87 ± 0.26 | 2.38 ± 0.19 |
| $\chi^{(2)}_{xxz}$ | 0.32 ± 0.11 | 0.28 ± 0.12 | 0.4 ± 0.16 |

### 4.2.2 Second-order nonlinearity of silicon nitride measured in waveguide configuration

Furthermore, we successfully demonstrated, for the first time, phased-matched second-harmonic generation in silicon nitride waveguides using these bulk nonlinearities. The mode dispersion engineering was performed for the achievement in phase-matching

while the waveguide width was varied (in both the simulation of model and the actual sample for measurements) to find the cross-over point where the effective index of the pump (1550nm) matched with the index of the generated second-harmonic (SH) field. According to the free-space results, a TM polarized SH can be expected using the $\chi^{(2)}_{zzz}$ tensor component and a TM type pump, at the same time, a TE second-harmonic signal could be also generated utilizing the component tensor of $\chi^{(2)}_{xxz}$ and a combination of TE and TM pump. Figure 4.2(a) and (b) shows the SEM images of the fabricated clad silicon nitride waveguides along with experimentally obtained results showing generated TE second-harmonic signals.

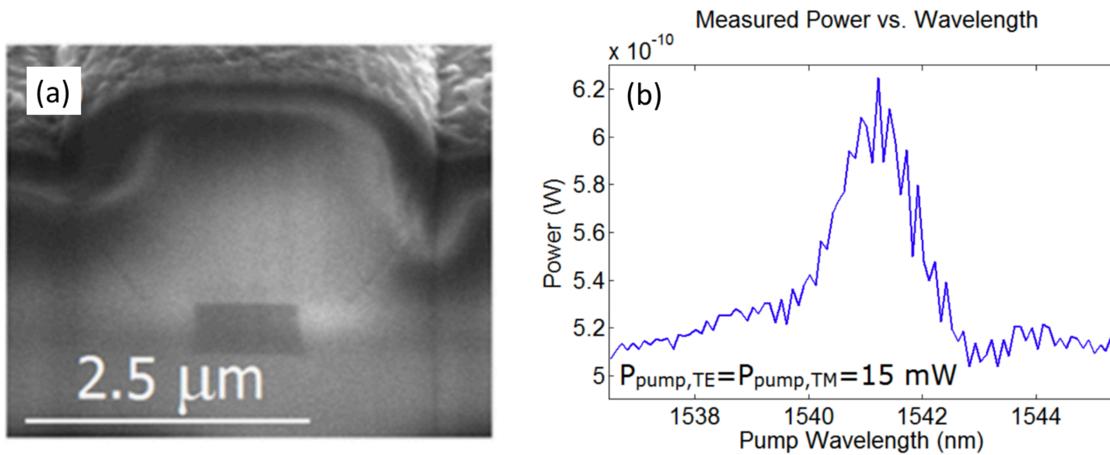


Figure 4.2: (a) SEM image of the silicon nitride waveguide. (b) Measured TE second-harmonic power generated in a 1070 nm-wide silicon nitride waveguide, as a function of the pump wavelength.

### 4.2.3 Enhanced second-order nonlinearity in silicon-rich nitride

In the previous chapters we have demonstrated bulk nonlinearities in silicon nitride thin films through both free-space and on-chip, in-waveguide measurements. The magnitude of nonlinearity was however low, with in waveguide measurements (at 1550nm) yielding values of $\chi^{(2)}$ lower than 1 pm/V. The origin of the bulk nonlinearity in these films

is not fully understood yet, however it is our hypothesis that the exhibited nonlinearities, both second- and third-order, would scale with the index of the deposited films. In order to verify the hypothesis, we modified the deposition recipe of PECVD machine, in terms of $SiH_4$ flow rate, to deposit three different films with different silicon ratios, with refractive index varying from 1.9 to 2.25.

## 4.3 Results

We will begin by examining the effect of the $SiH_4$ flow rate on the optical linear and nonlinear properties of silicon nitride thin films. In Table 4.2, the reader can see three different depositions of silicon nitride thin films, referred to as S1, S2, and S3. Throughout these three films the only deposition parameter allowed to vary was the flow rate of $SiH_4$, while the flow rate of $N_2$, the temperature, and the RF power were held constant. From this we can compare the refractive index of the three films, measured using the ellipsometry, with their composition. Examining this data, we see that as the flow rate of $SiH_4$ is increased the refractive index of the silicon nitride film also increases, illustrating that as the flow rate of $SiH_4$ increases, more silicon is introduced into the silicon nitride thin films. In order to verify this conclusion, we then examine the energy dispersive X-ray microanalysis of all three silicon nitride thin films, which will allow us to determine the ratio of Si to nitrogen ( Si/N ratio ) in each of the films as shown in figure 4.3. In figure 4.4, the blue and red bars represent the percentage of nitrogen and silicon in silicon nitride thin films, respectively. And an example of this measurement can be seen for S3 in the inset of figure 4.4(a), while the Si/N ratio for all three films extracted in this manner can

be seen in Table 4.2. The Si/N ratio of the three films can be seen to increase across the three films, S3 being nearly double that of S1, and therefore a larger optical nonlinearity can be expected.

In order to study the effect of silicon content on the optical nonlinearity of these thin films, a polarization dependent Makers fringes method was employed for both p- and s- polarized second-harmonic-generation (SHG) at a pump wavelength of 800 nm, the details of the setup can be found in Appendix C. The SHG intensity as a function of polarization angle for the p- polarized case can be seen in figure 4.4(b). Here it can be seen that as expected S3 presents an order larger SHG signal as compared to S1, demonstrating that silicon rich silicon nitride does indeed exhibit larger second-order nonlinearities than stoichiometric silicon nitride. Utilizing both the p- and s- polarized second harmonic generation signals, an example of which can be seen in figure 4.4(c) for S3, the tonsorial components of the nonlinear susceptibility of these three films can be extracted using Maker fringes analysis for the pump wavelength at 800 nm. The calculated results are presented in Table 4.2. In our experiment, S3 exhibited a 3.3 times large $\chi^{(2)}_{zzz}$ than S1 despite the fact that further optimization can be done.

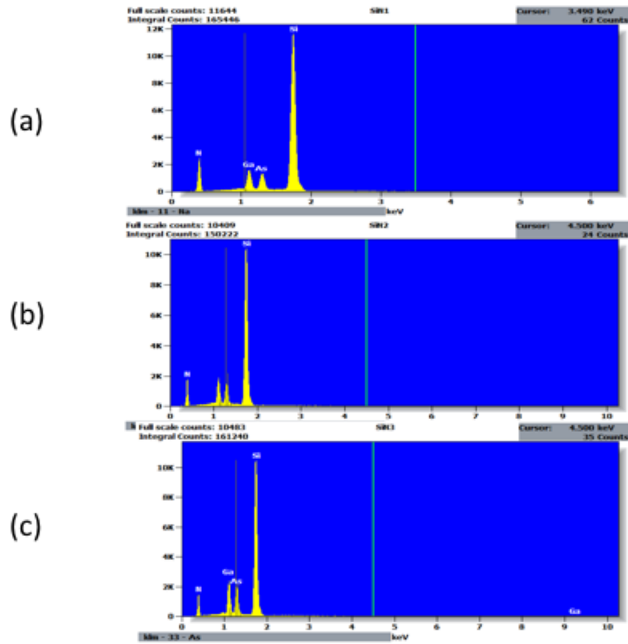


Figure 4.3: EDX results on the sample of (a) S1, (b) S2 and (c) S3.

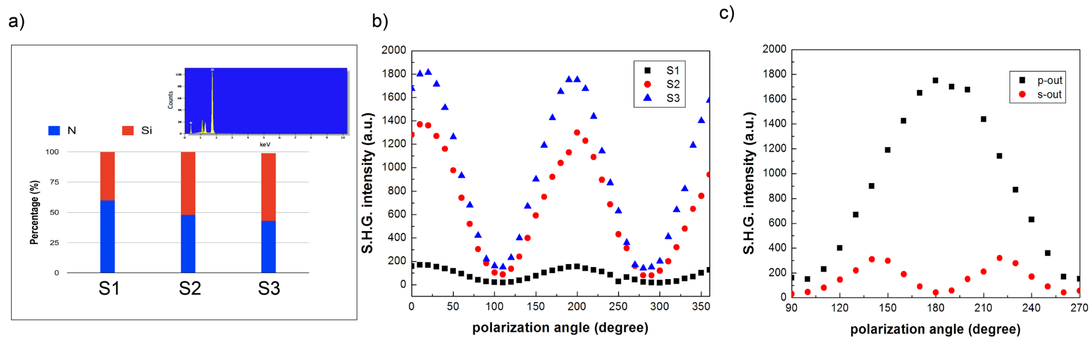


Figure 4.4: (a) Composition of sample S1, S2 and S3 investigated by energy dispersive X-ray (EDX) microanalysis, the inset figures is the example of measured EDX data on sample S3. (b) The p- (black squares) and s- (red squares) generated S.H.G. signals from S3 under variant incident polarization angles. (c) The p- (black squares) and s- (red squares) generated S.H.G. signals from S3 under variant incident polarization angles.

Table 4.2: The deposition recipes and measured properties of silicon nitride thin films.

| | $SiH_4$ flow rate (sccm) | Si/N ratio | Refractive index | $\chi^{(2)}_{zzz}$ (pmV) | $\chi^{(2)}_{zxx}$ |
|---|---|---|---|---|---|
| S1 | 180 | 0.7 | 1.9 | 2.4 | 0.4 |
| S2 | 276 | 1.05 | 2.08 | 5.8 | 1.1 |
| S3 | 500 | 1.3 | 2.25 | 8 | 1.9 |

To characterize the viability of these films for on-chip applications, in-waveguide passive optical measurements were performed to determine the propagation loss. The width of waveguide ranging from 500-1000 nm were deposited and patterned into coupled ring-resonators. The fabrication processes started with the silicon-on-insulator (SOI) wafers which consists of a 200 nm-thick device layer and 1 μm-thick buried oxide (BOX) layers.. Then a 400 nm of silicon-rich-nitride, was deposited through PECVD with a $SiH_4$ flow rate of 700 sccm. Waveguides with widths ranging from 500-1000 nm were then fabricated with coupled ring-resonators with coupling gaps ranging from 150-300 nm, using a combination of e-beam lithography (EBL) and the reactive ion etching (RIE) in an Oxford Plasmalab 100 using a $C_4F_8$ and SF6 plasma as reactive etching gas. Top-down SEM images of the fabricated waveguide structures are shown in figure 4.5. The fabrication of the devices were then completed with a top cladding layer of 1 μm-thick PECVD oxide.

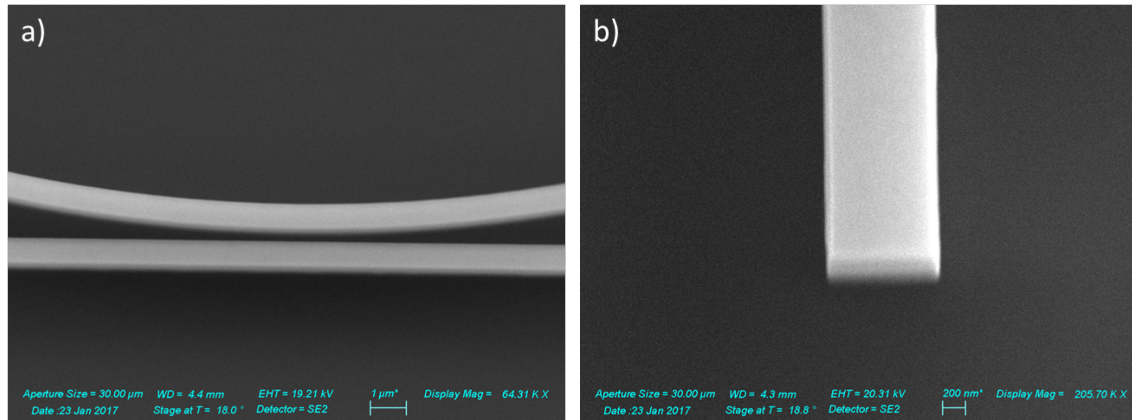


Figure 4.5: SEM micrograph of an unclad SRN waveguides showing the waveguide cross-section and the coupling region of the ring-resonators

To measure the propagation loss in the waveguide configuration, a fiber-in, free-space out setup was employed. The output of an near-IR agilent laser with a tunable range from 1465 to 1575 nm sources, was coupled into the silicon nitride waveguides by a polarization maintaining lensed-tapered fiber. The light emitted coming from the output side of waveguides was then collected by a metallic output objective, and the mode was magnified using two 4F systems of lenses. The collect transmitted light was detected and measured using an optical power meter, and the transmission spectrum, shown in figure 4.6, was obtained by continuously tuning the wavelength of the input of the laser.

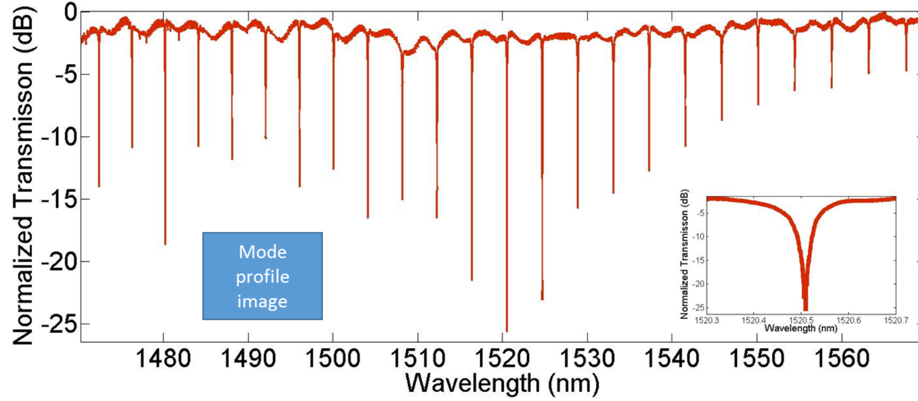


Figure 4.6: Normalized transmission of a 1um wide SRN waveguide coupled to a ring-resonator at a coupling gap of 250 nm. The inset shows the corresponding mode profile of the fundamental TE mode and a single resonance at 1520 nm, used to estimate the loss-coefficient of these waveguides.

The measured transmission spectra exhibiting periodic dips at each of the rings' resonant wavelengths, and the shapes and positions of these dips could be fit with Lorentzian curves for extracting the loss coefficients in the waveguides, which was determined to be around 10 dB/cm. It should be mentioned that the loss can be further improved via post-deposition annealing processes, however it's corresponding effect on the exhibited nonlinearity of the deposited films is still being studied.

## 4.4 Discussion

The value of the extracted $\chi^{(2)}$ coefficients from the in-waveguide measurements was $\chi^{(2)}_{zzz}$ ranging from 0.12-0.48 pm/V and $\chi^{(2)}_{xxz}$ ranging from 0.06-0.22 pm/V, where z is the direction which is normal to the surface of the thin films, and the $\chi^{(2)}$ values measured from free-space measurement is almost an order larger. The discrepancy between the values obtained from free-space and on-chip measurements is hypothesized to be because

of the highly dispersive nature of $\chi^{(2)}$, as well as the different mechanical and chemical conditions that the nitride film is exposed to during the waveguide fabrication process.

With the dispersion of the optical nonlinearities of silicon nitride in doubt, we decided to perform second harmonic generation experiments at two different wavelengths, 1040nm and 1550nm respectively. The measurement for reflective SHG details are described in the supplementary material and the setup is shown in figure 4.7(a). Samples S1, S2 and S3 are measured under same conditions including incident angles, spot size of the beam, average pump power and polarization states. The generated p-polarized SHG signals for all three thin films at pump wavelength of 1040 and 1550 nm are shown in figure 4.7(b). The sample S3, which has the highest silicon content provides largest SHG signal among threes samples at both wavelength. Interestingly, here a decrease in the SHG intensity from 1040nm to 1550nm of 20-30 times can be seen for all three samples, leading to a decrease of 4-5 times in the second-order nonlinearity.

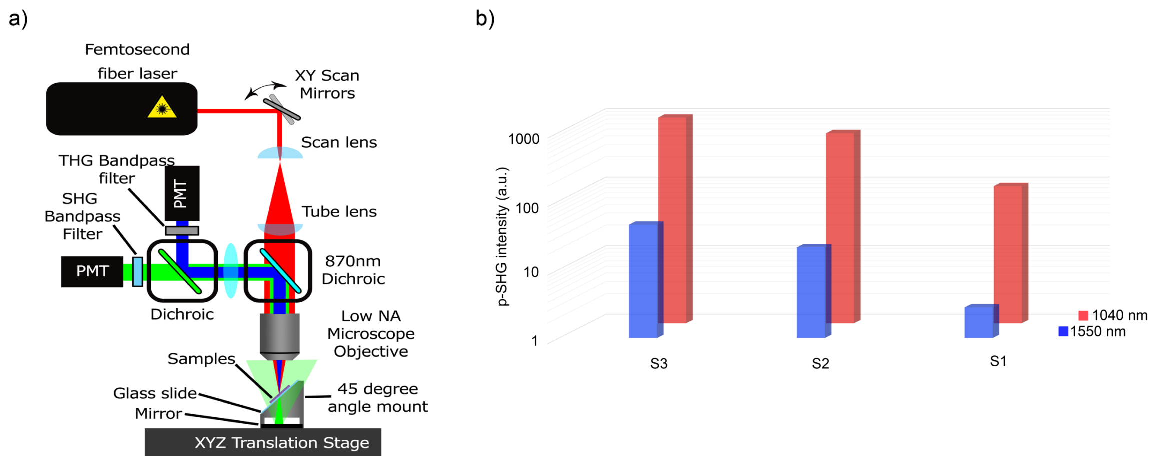


Figure 4.7: (a) Schematic of reflective second-harmonic generation setup. (b) Generated reflective p-SHG signals from samples at the wavelength of 1040 nm (red bars) and 1550 nm (blue bars), respectively.

## 4.5 Conclusion

To summarize, we have shown for the first time that the bulk $\chi^{(2)}$ in free-space measurements of silicon nitride thin films may be used in a CMOS-compatible integrated platform to achieve phase-matched second-harmonic generation in dispersion engineered waveguide geometries. By considering the polarizations of the optical modes relevant to the wavemixing process, we characterized two specific components of the $\chi^{(2)}$ tensor, $\chi^{(2)}_{zzz}$ and $\chi^{(2)}_{xxz}$. As new optical nonlinear material candidates continue to be considered for the advancement of integrated photonics, we believe that the characterization of material's nonlinear behaviors in both free-space and on-chip measurements will be critical in determining which material platform shows most promise for CMOS realization of a new generation of nonlinear optical devices. The silicon-rich nitride has been proved to exhibit an order larger second-order nonlinearity at 800 nm and also telecommunication range, 1550nm. However, it should be noticed that the second-order nonlinearity at longer wavelength (i.e., 1550 nm) is 5 times smaller than the values measured at 1040 nm, which should be taken into account for device design and telecommunication range. Most reported values is done at either 800 nm or 1064 nm. We emphasize our capability of measuring second-harmonic generation at both visible and 1550 nm, the most reliable and trustable way of direct characterization of nonlinear materials optical properties, not relying on slower and indirect measurement likes the commonly used electro-optic effect. The deposition techniques will be further optimized for pursuing low loss, large $\chi^{(2)}$ silicon-rich nitride films for fabricating on-chip nonlinear optic devices.

## Acknowledgments

This chapter contains material partly from "Observation of second-harmonic generation in silicon nitride waveguides through bulk nonlinearities" published at Optics Express by Matthew Puckett, Rajat Sharma, Hung-Hsi Lin, Mu-Han Yang, Felipe Vallini and Yeshaiahu Fainman. The dissertation author was co-author and in charge of measurements of second-order nonlinearity in silicon nitride in both free-space and in waveguide configuration. This part also contains materials from "On the nature of second-order nonlinearity in silicon nitride" which is in preparation for submission, the dissertation author is the first author of the manuscript.

# CHAPTER 5

# CONCLUSION AND FUTURE WORKS

This thesis summarizes the efforts in engineering the second-order nonlinearity in metamaterials based on CMOS-compatible dielectrics, semiconductors and metals, also in the study of nonlinearity in stoichiometry and silicon-rich nitride materials, all of them has great potential for the application in on-chip nonlinear optical components.

First, the engineered nonlinearity in the DSD materials was demonstrated using the generated fixed charges at dielectric/semiconductor interfaces, and the largest $\chi^{(2)}$ tensor was measured to be 8.5 pm/V, which is at the same level as some III-V materials such as aluminum nitride and gallium nitride. The mechanism of synthesized nonlinearity in DSD metamaterials is proved clearly that comes from EFISH effect, therefore, either increase of the fixed charge density or utilization of high $\chi^{(3)}$ material as semiconductor could efficiently push the value of effective $\chi^{(2)}$ higher. It is worthy to notify that the experimental results from my works mentioned are preliminary and not optimized yet, it is believed that with further optimization of the fabrication processes and the proper selection of composite materials, a customized metamaterial which exhibits the desired optical linear and nonlinear properties can be easily synthesized for specific application at different wavelength region.

Another concept utilizing the metal-semiconductor junction for engineering nonlinearity was also proposed in MSM metamaterials. It is proved that the effective $\chi^{(2)}$ in MSM metamaterial is proportional to the difference of work function between two used metals. The benefit of the MSM metamaterial is the tunability of the effective $\chi^{(2)}$ via external voltage applied, ranging from 10 to 40 pm/V, which provides this material the capability in switching applications. To increase the tunability of the MSM metamaterial, a-Si cane be replaced with other semiconductors pursing higher breakdown electric field such as silicon carbide towards a higher amplitude tuning range. With the capability of tuning the amplitude of the SHG signal, the concept of MSM metamaterials exhibit a great potential for many applications such as optical switching for free-space optical communication systems.

The works in silicon nitride and silicon-rich nitride provides a potentially low optical loss platform for on-chip nonlinear optical devices. It was found that the $\chi^{(2)}$ indeed exist in bulk of nitride thin films, which is proportional to the percentage of silicon within $SiN_x$. One important finds from my work is that the nonlinearity seems to be smaller at longer wavelength (i.e., 1550nm) than the $\chi^{(2)}$ measured at shorter wavelength (i.e., 1040 nm), which makes the modulators designed using this material very difficult. The future works on this project will be mainly focusing on the understanding of the $\chi^{(2)}$ source in silicon nitride thin films, and then explain theoretically the found about decrease of $\chi^{(2)}$ at longer wavelength.

The ability to construct nanoscale engineered nonlinear optical metamaterials that can be manufactured with CMOS compatible fabrication processes will have a profound impact on energy efficient and compact devices and photonic integrated circuits. The

proposed materials in this thesis will not only advance the basic science and technology of engineered nonlinear optical metamaterials, but also set an example for the investigation of physical phenomena where self-consistent treatment of electronic and optical material properties in conjunction with electromagnetics and nonlinear optical phenomena interactions becomes crucially important. I anticipate that the proposed nanoscale engineered nonlinear optical metamaterials and nitride based studies will find applications in data- and telecommunications, optical computing, and sensing systems.

.

# APPENDIX A

# C-V MEASUREMENT

## A.1 BACKGROUND

Capacitance-voltage (C-V) testing has been widely used for measuring semiconductor materials and properties such as metal-oxide-semiconductor field-effect transistors (MOSFET) structures and bipolar junction transistors (BJTs). As the applied voltage is applied, the capacitance of the structure is plotted as a function of voltage, which can be used for extracting the semiconductor properties or the defects within the dielectric layers [55].

## A.2 Materials and methods

To fabricate the MOS structure test samples for calculating $Q_f$ at dielectrics/a-Si interfaces, 100 nm thick a-Si is grown on a p-type silicon substrate first, followed by the deposition of a dielectric thin film (e.g., 120 nm of $SiO_2$ and 25 nm of $Al_2O_3$) using magnetron sputter at room temperature. Then, 100-nm-thick Al films are deposited with electron beam evaporation and patterned with photolithography processes on both top of dielectric and backside of silicon wafer as electrodes.

Agilent B1500A Semiconductor Device Analyzer is used for obtaining C-V curves by applying a 10 kHz AC electric field on the two Al electrodes. By observing the experimental flat-band voltage of the device and comparing it to the theoretical value, the

concentration of fixed charge in the dielectric may be calculated as [56]

$$Q_f = C_{dielectric}\left(\Delta\phi_{ms} - V_{FB}\right) \tag{S1}$$

where $C_{dielectric}$ is the dielectric capacitance per unit area, $\Delta\phi_{ms}$ is the difference in work function between the metal electrode and the semiconductor (and therefore the flat-band voltage in the absence of any dielectric non-idealities), and $V_{FB}$ is the measured flat-band voltage.

## Acknowledgments

The part of Appendix A contains the C-V measurement from “Characterizing the effects of free carriers in fully etched, dielectric-clad silicon waveguides” published at Applied Physics Letters drafted by Rajat Sharma, Matthew Puckett, Hung-Hsi Lin, Felipe Vallini and Yeshaiahu Fainman, the dissertation author is the co-author and in charge of C-V analysis on dielectric properties.

# APPENDIX B
# MAKER FRINGES SETUP

## B.1 BACKGROUND

The pump frequency light source is a Ti:Sapphire laser emitting 150 fs pulses with 80 MHz repetition rate at a center wavelength of 800 nm for performing Maker fringes setup, shown in figure S1. The polarization state is defined by a half-wave plate and a long pass filter with cut-off wavelength at 780 nm is set to filter out any signals from other sources in the range of interest. The sample is tilted and fixed at an angle of 45 degrees normal to the incident beam, which is focused with an 10x objective resulting in a beam size with a diameter of 12 μm on the surface of the sample. Two short wavelength pass filters and one band pass filter with a total optical density of 12 are inserted to filter out the pump light at ω (i.e., 800nm wavelength), ensuring that all photons collected by the photomultiplier (PMT) are at 2ω (i.,e., 400 nm wavelength) and consequently generated from the SHG process. The collimated SHG signal from the sample is separated into p-polarized and s-polarized by a polarizer for calculating the different components of the $\chi^{(2)}$ tensor. The detected signal in PMT is then read with an oscilloscope.

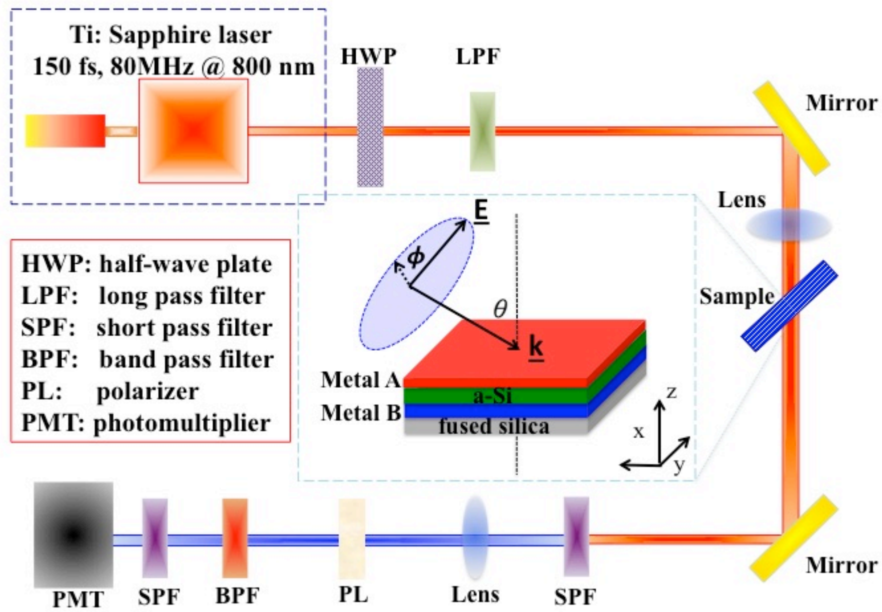


Figure S.1: Schematic of Maker fringes setup for optical characterization.

## B.2 Materials and methods

A commercial 500 μm thick X-cut quartz exhibiting nonlinear coefficient $\chi^{(2)}{}_{xxx}$ with 0.64 ± 8% pm/V is used for calibrating the system [57,58] and the absolute value of $\chi^{(2)}$ tensors from our samples are determined by comparing the generated SHG signals with the quartz sample under the same experimental conditions. The measurement errors originate mainly from the fluctuation of laser power due to the unstable humidity of environment (±5%), the fluctuation of readings from PMT resulting from the influence of background noises (±20%), and the non-ideal uniformity of deposited thin films (±10%). Besides, the possibility in counting error (±10%) of photons for PMT (Hamamatsu Inc., H11461-03) due to pulse overlapping described in the handbook is also taken into account.

We have included all these sources of error in the estimated $\chi^{(2)}$, and in order to

minimize these errors, the generated SHG intensities from quartz and DSD metamaterials are determined by the average of five different spots on each sample. The dummy sample of amorphous silicon deposited on sapphire and fused silica is also examined by X-ray diffraction (XRD), proving the fact that no crystalline silicon was deposited by sputter, the XRD results are shown in figure S2.

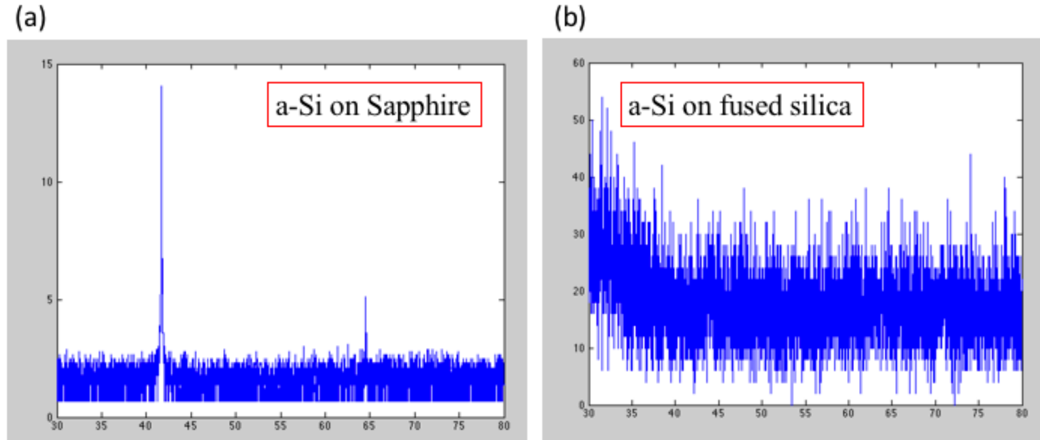


Figure S.2: EDX results of a-Si grow on (a) sapphire and (b) fused silica.

Following Herman's equation [59], three independent tensor components, $\chi^{(2)}_{zzz}$, $\chi^{(2)}_{xxz}$ and $\chi^{(2)}_{zxx}$ can be extracted by fitting the generated s- and p-polarized second-harmonic signals under variant polarization angle of pump incident laser. Since the a-Si has non-zero absorption coefficients at both the fundamental and second- harmonic fields, the complex index of refraction should be expressed as $\widetilde{n_m} = n_m(1 + i\kappa_m)$, where $n_m$ denotes the real part of refractive index and $\kappa_m$ represents the extinction coefficient of the materials at the frequency mω with m=1 and m=2 for the fundamental and second harmonic fields. Since the total thickness of DSD structures is small compared to incident wavelength, we use the effective medium approximation yielding the following expressions for the

determination of the effective refractive indices from different DSD metamaterials:

$$n_{eff} = \sqrt{\frac{\sum_i^s n_i^2 h_i}{h}} \tag{S2}$$

$$\kappa_{eff} = \sqrt{\frac{\sum_i^s \kappa_i^2 h_i}{h}} \tag{S3}$$

where $i = 1,2,3, \dots, s$, designate the composites in DSD structures, and $h_i$ is the thickness of the i-th layer. The real and imaginary part of refractive index from different dielectric and a-Si are measured using the Ellipsometer, yielding values in Table S1.

Table S.1: Real and imaginary part of refractive index for dielectrics and a-Si thin films measured using elliposometer at 400 nm and 800 nm.

| | Refractive index at 800nm | Refractive index at 400nm |
|---|---|---|
| $SiO_2$ | n=1.47 | n=1.45 |
| a-Si | n=3.93 κ=0.09 | n=4.3 κ=1.87 |
| $Al_2O_3$ | n=1.76 | n=1.78 |

## Acknowledgements

The Appendix B contains materials partly from “Synthesis of second-order nonlinearities in dielectric-semiconductor- dielectric metamaterials," published at Applied Physics Letters drafted by Hung-Hsi Lin, Mu-Han Yang, Rajat Sharma, Matthew Puckett, Christian Wurm, Sergio Montoya, Felipe Vallini, Eric Fullerton and Yeshaiahu Fainman. The dissertation author was the first investigator and author of this paper.

# APPENDIX C

# MAKER FRINGES ANALYSIS FOR MSM METAMATERIALS

## C.1 BACKGROUND

Since a-Si is an amorphous material, we assume that its third-order susceptibility tensor $\chi^{(3)}$ components are same as those of an isotropic material with $C_{\infty,v}$ space symmetry and thus has 21 nonzero elements, of which only 3 are independent:

$$yyzz = zzyy = zzxx = xxzz = xxyy = yyxx \quad (S4)$$
$$yzyz = zyzy = zxzx = xzxz = xyxy = yxyx \quad (S5)$$
$$yzzy = zyyz = zxxz = xzzx = xyyx = yxxy \quad (S6)$$
$$xxxx = yyyy = zzzz = zzxx + xzxz + xzzx \quad (S7)$$

The existence of a static electric field in z direction is expected to introduce effective $\chi^{(2)}$ tensor components: $\chi^{(2)}_{xxz}$, $\chi^{(2)}_{xzx}$, and $\chi^{(2)}_{zxx}$ and $\chi^{(2)}_{zzz}$ through the EFISH effect. We assume that the MSM structures are isotropic in the transverse (i.e., in-plane) direction and that multiple reflections within the thin films can be neglected due to the thin nature of constituent films (i.e., 5 and 25 nm) compared to the wavelength of pump light (i.e., 800nm). With the assistance of Maker fringes analysis, these non-zero $\chi^{(2)}$ tensor components of the MSM metamaterial: $\chi^{(2)}_{xxz}$, $\chi^{(2)}_{zxx}$ and $\chi^{(2)}_{zzz}$ can be determined from fitting the generated s- and p- polarized second-harmonic signal intensities at frequency $2\omega$ as a function of the polarization of the fundamental pump beam at frequency $\omega$, measured at a fixed angle of incidence, $\theta$. Also, since the thicknesses of MSM metamaterials are

much smaller than the wavelength of the pump beam, it is justified to use the effective medium theory for determining the three non-zero components of $\chi^{(2)}$ tensor in all MSM metamaterial structures. By neglecting multiple reflections within each layer, the transmitted p- and s- polarized second- harmonic signals with energy of 2ω can be expressed as:

$$P_{2\omega}^{s/p} = \frac{2\left((\sin(\phi))^2\left(t_{af}^{(p)}\right)^2 + (\cos(\phi))^2\left(t_{af}^{(s)}\right)^2\right)^2\left(T_{fs}^{(s/p)}\right)^2\left(T_{sa}^{(s/p)}\right)^2}{(n_2\cos(\theta_2))^2 cA\varepsilon_0} P_{1\omega}^2\left(\frac{2\pi}{\lambda}L\right)^2 d_{eff,s/p}^2 \times exp\left(-2(\delta_1+\delta_2)\right)\frac{(\sin\Psi)^2 + (\sinh X)^2}{\Psi^2 + X^2} \tag{S8}$$

Here, following Herman's notations, $P_{1\omega}$ and $P_{2\omega}$ denote the power at fundamental and second harmonic frequency, respectively, and the superscript s/p represents the state of polarization; $\phi$ is the angle of incidence for fundamental frequency beam while $\phi$ at 0° and 90° represent s- and p- polarized respectively; *t* and *T* are Fresnel transmission coefficients for the fundamental field at frequency, ω and second harmonic field at frequency, 2ω, respectively; the subscripts *af*, *fs* and *sa* stand for interfaces between air (a), f (film) and s (substrate); c is the speed of light in vacuum; A is the area of the spot size of the fundamental beam focused on samples surfaces; $\varepsilon_0$ is the absolute permittivity of free space; L is the thickness of MSM structures; λ is the wavelength of incident fundamental laser beam, which is set at 800 nm in our experiments. The incidence angle, $\theta_m$ inside MSM structure can be estimated using Snell's law $\sin\theta_m = \frac{1}{n_m}\sin\theta$ for the fundamental m=1 and second harmonic m=2 beams. Both a-Si and metals have non-zero absorption coefficients at the fundamental and second- harmonic fields. The complex index of refraction can be expressed as $\widetilde{n_m} = n_m(1+i\kappa_m)$, where $n_m$ denotes the real part of

refractive index and $\kappa_m$ represents the extinction coefficient of the materials at the frequency mω with m=1 and m=2 for the fundamental and second harmonic fields. Since the total thickness of MSM structures is small compared to incident wavelength, we use the effective medium approximation yielding the following expressions:

$$n_{eff} = \sqrt{\frac{\sum_i^s n_i^2 h_i}{h}} \tag{S9}$$

$$\kappa_{eff} = \sqrt{\frac{\sum_i^s \kappa_i^2 h_i}{h}} \tag{S10}$$

where $i = 1,2,3, \dots, s$, designate the composites in MSM structures, and $h_i$ is the thickness of the i-th layer. The real and imaginary part of refractive index from different metals and a-Si are measured with Rudolph Auto EL Ellipsometer, yielding values in Table S2.

Table S.2: Real and imaginary part of refractive index for metal and a-Si thin films measured using elliposometer at 400 nm and 800 nm.

| | Refractive index at 800nm | Refractive index at 400nm | | Refractive index at 800nm | Refractive index at 40nm |
|---|---|---|---|---|---|
| Silica | n=1.46 κ=0 | n=1.44 κ=0 | Pt | n=2.61 κ=5.2 | n=1.83 κ=2.1 |
| a-Si | n=3.93 κ=0.09 | n=4.3 κ=1.87 | Ni | n=1.35 κ=2.8 | n=2.42 κ=4.41 |
| Al | n=2.68 κ=7.81 | n=0.43 κ=4.42 | | | |

## C.2 Materials and methods

Following quantities shown in equation (S10) represents the influences of imaginary part of refractive index on generated SHG intensity for absorbing nonlinear materials. The physical meaning can be found in details from Herman's works:

$$\delta_m = \frac{2\pi L}{\lambda}\frac{n_m \kappa_m}{\cos\theta_m} \tag{S11}$$

$$X = \delta_1 + \delta_2 \tag{S12}$$

$$\Psi = \frac{2\pi L}{\lambda}(n_1 \cos\theta_1 - n_2 \cos\theta_2) \tag{S13}$$

The relation between effective susceptibility $d_{eff,s/p}$ and three $\chi^{(2)}$ tensors is expressed as:

$$d_{eff}^{p} = -\frac{1}{2}(\chi_{xzx}\cos\theta_2 \sin 2\theta_1 (\sin\phi')^2 + \chi_{zxx}\sin\theta_2 ((\cos\theta_1 \sin\phi')^2 + (\cos\phi')^2) + \chi_{zzz}\sin\theta_2 (\sin\theta_1 \sin\phi')^2) \quad \text{(S14)}$$

$$d_{eff}^{s} = -\frac{1}{2}\chi_{xzx}\sin\theta_1 \sin 2\phi' \quad \text{(S15)}$$

The polarization angle in the thin film stacks $\phi'$ can be expressed by:

$$\tan\phi' = \tan\phi \times \frac{t_{af}^{p}}{t_{af}^{s}} \quad \text{(S16)}$$

The detected s- and p-polarized SHG intensities are used to determine the effective susceptibility $d_{eff,s/p}$ by fitting measured signals under variant polarization states of incident fundamental beam. Based on (S14) to (S16), absolute value of three components of $\chi^{(2)}$ tensor can be extracted in the bulk of all MSM metamaterials.

## C.3 Analysis of the effect of photocurrent on the built-in electric field within a-Si layer

The induced effective $\chi^{(2)}$ in our MSM structures comes from the engineered non-zero static electric field within the semiconductor (i.e., a-Si) layer. Since the SHG measurements were carried out using optical fields with photon energies (i.e., 1.55 e.V.) larger than bandgap of a-Si (i.e., 1.1 e.V.), we need to consider the effect of light induced free carrier generation, which may affect the magnitude of the built-in electric field in a-Si, and, consequently, the induced effective $\chi^{(2)}$. In order to quantify the influence of the generated photocurrent on the built-in electric field, we performed I-V measurements (see figure S2(a)) with and without illumination at the pump wavelength on the sample with the MSM structure consisting of Ni/a-Si/Al.

An external voltage V is applied across patterned 1mm x 1mm Ni metal squares and bottom Al metal film. The pump beam is focused on the patterns with a 10x objective lens resulting in a spot size with radius of 20 μm. The I-V characteristics are then studied under variant illumination conditions with a Keithley model 2400. Pump light with average power ranging from 12.5 to 200 mW is illuminated on the MSM structure and the I-V characteristics are shown in figure S2(b). By analyzing the I-V curves, electrical properties such as the serial resistance of the MSM structure, dark current, photocurrent and the Schottky barrier height between metals and a-Si can be calculated [60,61]. These results are summarized in Table S3.

The serial resistance of the MSM stack is barely affected by the laser beam in our experiments. The measured dark current in the MSM structure is determined to be 43.8 nA, whereas the photocurrent can be an order of magnitude larger than the dark current. The measured photocurrent is 401 nA when illuminated by a pump beam with an average power of 100 mW, identical to the condition of our experiments. This large induced photocurrent could lower the Schottky barrier height through image force effect [62], in other words, lower the built-in electric field within a-Si, hence affecting the induced optical nonlinearity and thereby lead to an inaccuracy in the estimated values of $\chi^{(2)}$ tensors. Comparing the Schottky barrier height under dark to that under illumination with a power of 100 mW, we observed a reduction by 15%, confirming the fact that the image force effect does indeed lower the barrier in our case. We then simulate the influence of this effect on the built-in electric field using Silvaco tool, and determine that the decrease in the value of the induced field due to the generated photocurrent is about 10%. In summary, we conclude that the

pump-generated photocarriers have a minor effect on the measured effective $\chi^{(2)}$ in our MSM structure.

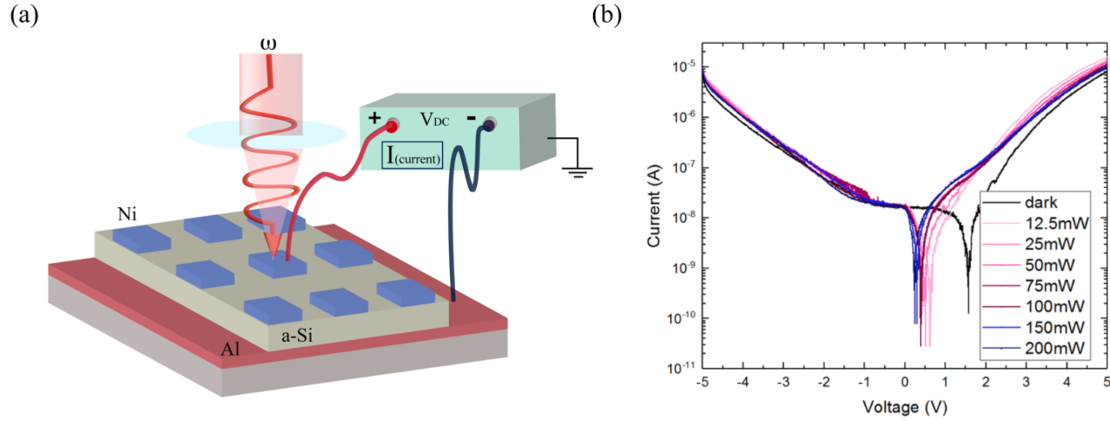


Figure S.3: (a) Schematic of the patterned MSM stack for measurement of I-V behaviors under different illumination conditions. (b) I-V behaviors without (black) and with illumination under variant of average power.

Table S.3: Electrical properties of a-Si layer under variant illumination conditions.

| | Serial resistance (Ohm) | Dark current (nA) | Photocurrent (nA) | Schottky barrier height (V) |
|---|---|---|---|---|
| Dark | 4.629 k | 43.8 | - | 0.69 |
| 50mW | 4.612 k | - | 193 | 0.63 |
| 100mW | 4.609 k | - | 401 | 0.61 |
| 150mW | 4.560 k | - | 595 | 0.6 |
| 200mW | 4.520 k | - | 812 | 0.59 |

## Acknowledgments


The Appendix C contains material from “Electronic Metamaterials with Tunable Second-order Optical Nonlinearities” published at Scientific Reports in 2017 drafted by Hung-Hsi Lin, Felipe Vallini, Mu-Han Yang, Rajat Sharma, Matthew Puckett, Christian

Wurm, Sergio Montoya, Eric Fullerton and Yeshaiahu Fainman. The dissertation author was the first investigator and author of this paper.

## BIBLIOGRAPHY


[1] J. Cardenas, C. B. Poitras, J. T. Robinson, K. Preston, L. Chen, and M. Lipson, "Low loss etchless silicon photonic waveguides," *Opt. Express*, vol. 17, Issue 6, pp. 4752–4757, 2009.

[2] G. Z. Mashanovich, M. M. Miloševic, M. Nedeljkovic, N. Owens, B. Xiong, E.J. Teo and Y. Hu, "Low loss silicon waveguides for the mid-infrared," *Opt. Express*, vol. 19, Issue 8, pp. 7112–7119, 2011.

[3] C. Malgrange, C. Ricolleau, and M. Schlenker, "Symmetry and Physical Properties of Crystals," (Springer, 2014).

[4] R. Sharipov, "Quick introduction to tensor analysis," preprint *arXiv:math/0403252* (2004).

[5] R. S. Jacobsen, K. N. Anderson, P. I. Borel, J. F. Pedersen, L. H. Frandsen, O. Hansen, M. Kristensen, A. V. Lavrinenko, G. Moulin, H. Ou, C. Percheret, B. Zsigri, and A. Bjarklev "Strained silicon as a new electro-optic material," *Nature*, vol. 441, pp. 199-202, May 2006.

[6] B. Chmielak, M. Waldow, C. Matheisen, C. Ripperda, J. Bolten, T. Wahlbrink, M. Nagel, F. Merget, and H. Kurz, "Pockels effect based fully integrated, strained silicon electro-optic modulator," *Opt. Express* vol. 19, pp.17212–17219, 2011.

[7] B. Chmielak, C. Matheisen, C. Ripperda, J. Bolten, T. Wahlbrink, M. Waldow, and H. Kurz, "Investigation of local strain distribution and linear electro-optic effect in strained silicon waveguides," *Opt. Express* vol. 21, pp.25324–25332, 2013.

[8] P. Damas, X. Le Roux, D. Le Bourdais, E. Cassan, D. Marris-Morini, N. Izard, T. Maroutian, P. Lecoeur, and L. Vivien, "Wavelength dependence of Pockels effect in strained silicon waveguides," *Opt. Express* vol. 22, pp. 22095–22100, 2014.

[9] M. Puckett, J. Smalley, M. Abashin, A. Grieco, and Y. Fainman, "Tensor of the second-order nonlinear susceptibility in asymmetrically strained silicon waveguides: Analysis and experimental validation," *Opt. Lett.* Vol. 39, pp. 1693–1696, 2014.

[10] P. Damas, X. L. Roux, D. Le Bourdais, E. Cassan, D. Marris-Morini, N. Izard, T. Maroutian, P. Lecoeur, and L. Vivien, "Wavelength dependence of Pockels effect in strained silicon waveguides, "*Opt. Express* vol. 22, pp. 22095-22100, 2014.

[11] M. Borghi, M. Mancinelli, F. Merget, J. Witzens, M. Bernard, M. Ghulinyan, G. Pucker, and L. Pavesi, "High frequency electro-optic measurement of strained silicon racetrack," *Opt. Lett.* Vol. 40, issue 22, pp. 5287–5290, 2015.

[12] C. Schriever, F. Bianco, M. Cazzanelli, M. Ghulinyan, C. Eisenschmidt, J. Boor, A. Schmid, J. Heitmann, L. Pavesi, and J. Schilling,“ Second-Order Optical Nonlinearity in Silicon Waveguides: Inhomogeneous Stress and Interfaces ”*Adv. Opt. Mater.* vol. 3, p.129, 2014.

[13] T. Ning, H. Pietarinen, O. Hyvarinen, J. Simonen, G. Genty, and M. Kauranen, “Strong second-harmonic generation in silicon nitride films,” *Appl. Phys. Lett.* vol. 100, issue 16, p.161902, 2012.

[14] M. Nedeljkovic, R. Soref, and G. Mashanovich, “Free-carrier electrore- fraction and electroabsorption modulation predictions for silicon over the 1-14-um infrared wavelength range,” *Photonics J.* vol. 3, pp.1171–1180, 2011.

[15] O. A. Aktsipetrov, A. A. Fedyanin, V. N. Golovkina, and T. V. Murzina, “Optical second-harmonic generation induced by a dc electric field at the Si–SiO2 interface, ” *Opt. Lett.* Vol. 19, issue 18, pp. 1450–1452, 1994.

[16] O. A. Aktsipetrov, A. A. Fedyanin, E. D. Mishina, and A. N. Rubtsov, “dc-electric-field-induced second-harmonic generation in Si(111)-$SiO_2$-Cr metal-oxide-semiconductor structures,” *Physical Review B* vol. 54. Pp.1825-1831, 1996.

[17] J. S. Levy, M. A. Foster, A. L. Gaeta, and M. Lipson, “Harmonic generation in silicon nitride ring resonators,” *Opt. Express* vol.19 issue 12, pp. 11415–11421, 2011.

[18] A. Kitao, K. Imakita, I. Kawamura and M. Fujii,“An investigation into second harmonic generation by Si-rich SiNx thin films deposited by RF sputtering over a wide range of Si concentrations*,” J. Phys. D: Appl. Phys* vol 47, p215101, 2014

[19] K. Koskinen, R. Czaplicki, A. Slablab, T. Ning, A. Hermans, B. Kuyken, V. Mittal, G. S. Murugan, T. Niemi, R. Baets, and M. Kauranen, “Enhancement of bulk second-harmonic generation from silicon nitride films by material composition,” *Opt. Lett.* Vol. 42, issue 23, pp. 5030–5033, 2017.

[20] J. B. Khurgin, T. H. Stievater, M. W. Pruessner, and W. S. Rabinovich, “On the origin of the second-order nonlinearity in strained Si–SiN structures, ” *Journal of the Optical Society of America B*, vol. 32, issue 12, pp. 2494-2499, 2015

[21] M. W. Puckett, R. Sharma, H. Lin, M. Yang, F. Vallini, and Y. Fainman, “Observation of second-harmonic generation in silicon nitride waveguides through bulk nonlinearities, ” *Opt. Express* vol. 24, issue 15, pp. 16923–16933, 2016.

[22] Rajat Sharma, Matthew W. Puckett, Hung-Hsi Lin, Felipe Vallini, and Yeshaiahu Fainman, “Characterizing the effects of free carriers in fully-etched, dielectric-clad silicon waveguides, ” *Appl. Phys. Lett.* vol. 106, p.241104, 2015.

[23] R. Sharma, M. W. Puckett, H. Lin, A. Isichenko, F. Vallini, and Y. Fainman, “Effect of dielectric claddings on the electro-optic behavior of silicon waveguides” *Opt. Lett.* Vol. 41, issue 6, pp. 1185–1188, 2016.

[24] P. Rabiei, J. Ma, S. Khan, J. Chiles, and S. Fathpour, “Heterogeneous lithium niobate photonics on silicon substrates,” *Opt. Express* vol. 21, issue 21, pp. 25573–25581, 2013.

[25] R. W. Boyd, *Nonlinear Optics* (Academic, San Diego, CA), 2003.

[26] E. Wooten, K. Kissa, A. Yi-Yan, E. Murphy, D. Lafaw, P. Hallemeier, D. Maack, D. Attanasio, D. Fritz, G. McBrien, and D. Bossi, “A review of lithium niobate modulators for fiber-optic communications systems,” Member, IEEE, *J. Sel. Top. Quantum Electron* vol. 6, pp.69-82, 2000.

[27] D. Bottomley, G. Lupke, C. Meyer, and Y. Makita,” Exact separation of surface and bulk contributions to anisotropic second-harmonic generation from cubic centrosymmetric media,” *Opt. Lett*. vol. 20, p.453, 1995.

[28] H. Tom, T. Heinz, and Y. Shen, “Second-Harmonic Reflection from Silicon Surfaces and Its Relation to Structural Symmetry,” *Phys. Rev. Lett*. vol. 51, p.1983 (1983).

[29] I. Kawamura, K. Imakita, A. Kitao, and M. Fujii, “Second-order nonlinear optical behavior of amorphous SiOx thin films grown by sputtering” *J. Phys. D: Appl. Phys.* Vol.48, p.395101, 2015.

[30] L. Alloatti, C. Kieninger, A. Froelich, M. Lauermann, T. Frenzel, K. Kohnle, W. Freude, J. Leuthold, M. Wegener, and C. Koos, “Second-order nonlinear optical metamaterials: ABC-type nanolaminates,” *Appl. Phys. Lett*. vol. 107, p.121903, 2015.

[31] E. Pshenay-Severin, A. Chipouline, J. Petschulat, U. Hubner, A. Tunnermann, and T. Pertsch, “Optical properties of metamaterials based on asymmetric double-wire structures, ”*Opt. Express* vol. 19, p.6269, 2011.

[32] M. Gentile, M. Hentschel, R. Taubert, H. Guo, H. Giessen, and M. Fiebig, “Investigation of the nonlinear optical properties of metamaterials by second harmonic generation,” *Appl. Phys. B* vol. 105, p.149, 2011.

[33] M. Larciprete, A. Belardini, M. Cappeddu, D. Ceglia, M. Centini, E. Fazio, C. Sibilia, M. Bloemer, and M. Scalora, “Second-harmonic generation from metallodielectric multilayer photonic-band-gap structures,” *Phys. Rev. A* vol. 77, p.013809, 2008.

[34] W. Ding, L. Zhou, and S. Chou, “Enhancement and electric charge-assisted tuning of nonlinear light generation in bipolar plasmonics,” *Nano Lett.* vol. 14, p.2822, 2014.

[35] S. Clemmen, A. Hermans, E. Solano, J. Dendooven, K. Koskinen, M. Kauranen, E. Brainis, C. Detavernier, and R. Baets, “Atomic layer deposited second-order nonlinear optical metamaterial for back-end integration with CMOS-compatible nanophotonic circuitry” *Opt. Lett.* vol. 40, p.5371, 2015.

[36] T. Baehr-Jones, M. Hochberg, and A. Scherer, “Photodetection in silicon beyond the band edge with surface states,” *Opt. Express* vol. 16, p.1659, 2008.

[37] B. Jalali and S. Fathpour, "Silicon photonics," *Journal of Lightwave Technology* vol. 24, pp.4600-4615, 2006.

[38] R. Soref, "Mid-infrared photonics in silicon and germanium," *Nature Photonics* vol. 4, pp.495-497, 2010.

[39] M. Dinu, F. Quochi, and H. Garcia, "Third-order nonlinearities in silicon at telecom wavelengths," *Appl. Phys. Lett*. vol. 82, p.2954, 2003.

[40] A. Bristow, N. Rotenberg, and H. van Driel, "Two-photon absorption and Kerr coefficients of silicon for 850-2200 nm," *Appl. Phys. Lett*. vol. 90, p.191104, 2007.

[41] R. Sharipov, "Quick introduction to tensor analysis," *arXiv:math/0403252*, 2004.

[42] H. Lin, M. Yang, R. Sharma, M. W. Puckett, S. Montoya, C. D. Wurm, F. Vallini, E. E. Fullerton, and Y. Fainman, "Synthesis of second-order nonlinearities in dielectric-semiconductor-dielectric metamaterials," Appl. Phys. Lett. vol. 110, p.113103, 2017.

[43] See www.lumerical.com to access the product description, manual and example files for Lumerical Solutions, Inc’s finite-difference time-domain (FDTD) simulation tool.

[44] J. Matres, G. Ballesteros, P. Gautier, J. Fedeli, J. Mart, and C. Oton, “High nonlinear figure-of-merit amorphous silicon waveguides” *Opt. Express* vol. 21, p.3932, 2013.

[45] A. Bristow, N. Rotenberg, and H. Driel, “Two-photon absorption and Kerr coefficients of silicon for 850 – 2200 nm,” *Appl. Phys. Lett.* vol. 90, p.191104, 2007.

[46] G. M. Barrow, “The Structure of Molecules,” (*W. A. Benjamin*), 1963.

[47] A. Beiser, “Perspective of Modern Physics,” (*McGraw-Hill*), 1969.

[48] J. Smalley, F. Vallini, S. Shahin, B. Kanté, and Y. Fainman, "Gain-enhanced high-k transmission through metal-semiconductor hyperbolic metamaterials," *Opt. Mater. Express* vol. 5, p.2300, 2015.

[49] A. Haija, W. Freeman, and T. Roarty, "Effective characteristic matrix of ultrathin multilayer structures," *Optica Applicata* vol. 36, pp.39-50, 2006.

[50] K. Ikeda, R. E. Saperstein, N. Alic, and Y. Fainman, "Thermal and Kerr nonlinear properties of plasma- deposited silicon nitride/ silicon dioxide waveguides," *Opt. Express,* vol. 16, issue 17, pp.12987–12994, 2008.

[51] C. Torres-Torres, A. López-Suárez, L. Tamayo-Rivera, R. Rangel-Rojo, A. Crespo-Sosa, J. C. Alonso, and A. Oliver, "Thermo-optic effect and optical third order nonlinearity in nc-Si embedded in a silicon-nitride film," *Opt. Express* vol. 16, issue 22, pp.18390–18396, 2008.

[52] D. Moss, R. Morandotti, A. Gaeta, and M. Lipson, "New CMOS-compatible platforms based on silicon nitride and Hydex for nonlinear optics," *Nat. Photonics,* vol. 7, issue 8, pp.597–607, 2013.

[53] J. Levy, A. Gondarenko, M. Foster, A. Turner-Foster, A. Gaeta, and M. Lipson, "CMOS-compatible multiple-wavelength oscillator for on-chip optical interconnects," *Nat. Photonics* vol. 4, issue 1, pp.37–40, 2010.

[54] S. Khan, J. Chile, J. Ma, and S. Fathpour, "Silicon-on-nitride waveguides for mid- and near-infrared integrated photonics," *Appl. Phys. Lett*. vol.102, issue 12, p.121104, 2013.

[55] R. Castagne and A. Vapaille, "Apparent interface state density introduced by the spatial fluctuations of surface potential in a M.O.S. structure," *Electron. Lett*. vol. 6, pp.691–694, 1970.

[56] S. Dauwe, J. Schmidt, A. Metz, and R. Hezel, "Fixed charged density in silicon nitride films on crystalline silicon surfaces under illumination," *Photovoltaic Specialists Conference IEEE*, pp. 162–165, 2002.

[57] N. Sanford, A. Davydov, D.Tsvetkov, A.Dmitriev, S. Keller, U. Mishra, S. DenBaars, S. Park, J. Han,and R. Molnar, "Measurement of second order susceptibilities of GaN and AlGaN," *Journal of applied physics* vol. 97, p.053512 , 2005.

[58] I. Shoji, T. Kondo, A. Kitamoto, M. Shirane, and R. Ito," Absolute scale of second-order nonlinear-optical coefficients" *J. Opt. Soc. Am. B* vol. 14, p.2268, 1997.

[59] W. Herman and L. Hayden, “Maker fringes revisited: second-harmonic generation from birefringent or absorbing materials” *J. Opt. Soc. Am. B* vol. 12, p.416, 1995.

[60] R. F. Schmitsdorf, T. U. Kampen, and W. Mönch, “Explanation of the linear correlation between barrier heights and ideality factors of real metal-semiconductor contacts by laterally nonuniform Schottky barriers,” *Journal of Vacuum Science & Technology B: Microelectronics and Nanometer Structures Processing, Measurement, and Phenomena* vol. 15, pp.1221-1226, 1997.

[61] L. F. Wagner, R. F. Young, and A. Sugerman, “A note on the correlation between the Schottky-diode barrier height and the ideality factor as determined from IV measurements,” *IEEE Electron Device Letters* vol. 4, pp.320-322, 1983.

[62] J. M. Andrews, and M. P. Lepselter, “Reverse current-voltage characteristics of metal-silicide Schottky diodes,” *Solid-State Electronics* vol. 13, pp.1011-1023, 1970.